DETECTION OF IN-FLIGHT ICING THROUGH THE ANALYSIS OF HYDROMETEORS WITH A VERTICALLY POINTING RADAR

by

Jennifer Lilly

Department of Atmospheric and
Oceanic Sciences McGill University,
Montreal, Quebec.

A thesis submitted to McGill University in partial fulfillment of the requirements of the degree of Masters of Science.

August, 2004

Abstract

Most aircraft icing accidents take place in the vicinity of an airport. As a result, identifying hydrometeors in a vertical column above the airport, especially the supercooled liquid water (SLW) that causes icing, is a crucial step in reducing the number of icing accidents. This study aims to provide a diagnosis of icing condition in the vicinity of an airport using a Vertically Pointing Radar (VPR).

The VPR is an X-band Doppler radar developed at McGill University that measures reflectivity, Doppler velocity, and the distribution of hydrometeor fall speeds. With these variables, five classification algorithms can be applied to identify the location of the melting layer, rain, drizzle, rime, and snow. Then, from the distribution of fall speeds, modes, or peaks in the power returned can be identified to provide information about regions of mixed precipitation. The existence of more than one mode is a good indication of mixed precipitation and a hidden type of hydrometeors, often associated with SLW. Once the precipitation has been identified, the Snow Flux Gradient and Snow Density Gradient algorithms are applied to the frozen precipitation to calculate the total amount of liquid water content (LWC).

When combined into one system and run continuously over time the 8 algorithms in this study will be able to provide a timely, affordable, and valuable warning as to the level and extent of icing conditions occurring in the airport region.

Résumé

La plupart des accidents de givrage d'avion ont lieu à proximité d'un aéroport. Pour en réduire le nombre, il est crucial d'identifier la nature des hydrométéores, et plus particulièrement la présence d'eau surfondue (SLW) qui cause le givrage au-dessus de l'aéroport. Dans cette étude, notre but est de fournir une technique pour diagnostiquer les conditions de givrage à proximité d'un aéroport à l'aide d'un radar à visée verticale (VPR).

Le VPR est un radar Doppler en bande X, développé à l'université McGill, qui mesure la réflectivité, la vitesse Doppler et la distribution des vitesses de chute des hydrométéores. Sur ces observations, cinq algorithmes de classification peuvent être appliqués pour localiser la bande brillante, les zones de pluie, de bruine, de givre, et de neige. Ensuite, on utilise les modes (ou les crêtes) de la distribution des vitesses de chute, pour caractériser les régions de précipitation mixte. La présence de plusieurs modes est une bonne indication de précipitation mixte et d'un type caché d'hydrométéores, comme la SLW. Une fois que le type de précipitation a été identifié, des algorithmes de gradient de flux de neige et de gradient de densité de neige sont appliqués à la précipitation solide pour calculer le contenu en eau liquide.

Toute cette procédure composée de 8 algorithmes permettra de mettre en place à l'aéroport un système d'alerte, en temps réel, robuste et peu coûteux pour les conditions givrantes.

Acknowledgements

I would like to express sincere appreciation to Professor Frédéric Fabry for his patience, advice, and encouragement throughout this project. I am also indebted to the members of the radar group for their weekly advice and expertise, as well as Professor Henry Leighton who gave me the chance to start this project. In addition, special thanks to Wanda Szyrmer who provided invaluable advice on the subject, and was a great office mate. Thanks again to my classmates who helped me all along the way with programming details and editing, especially Edwin Campos, Eduart Haruni, Andy Way, and Erin Roberts. Finally thanks to my parents and friends for their love, support, and help through all the stages of this project.

Table of Contents

Acronyms

AIRS: Alliance Icing Research Study

AIRMET: Airman's Meteorological Information

AVISA: Airport Vicinity Icing and Snow Advisor

ADWICE: Advanced Diagnosis and Warning System for Aircraft Icing Environments

CIP: Current Icing Product

FAA: Federal Aviation Administration

FIP: Forecast Icing Product

GOES: Geostationary Operational Environmental Satellite

GRC: Glenn Research Center

GRIDS: Ground-Based Remote Icing Detection System

ILWC: Integrated Liquid Water Content

LWC: Liquid Water Content

M-P DSD: Marshall- Palmer Drop Size Distribution

MSC: Meteorological Service of Canada

NASA: National Aeronautics and Space Administration

NCAR: National Center for Atmospheric Research

NIRSS: NASA's Icing Remote Sensing System

NOAA: National Oceanic and Atmospheric Administration

NSF: National Science Foundation

NTSB: National Transportation Safety Board

PIREP: Pilot Reports

POSS: Precipitation Occurrence Sensor System

RAP: Research Application Program

RUC-II: Rapid Update Cycle 2 Model

SIGMA: System of Icing Geographic identification in Meteorology for Aviation

SDG: Snow Density Gradient

SFG: Snow Flux Gradient

SLW: Supercooled Liquid Water

TC: Transport Canada

UTC: Universal Time

VPR: Vertically Pointing Radar

WSDDM: Weather Support for De-Icing Decision Making

ZV: Reflectivity Velocity relationship

List of Figures

Chapter 1

Introduction

1.1 Dangers of Aircraft Icing and Study Motivation

In the 100 years since that December day in 1903, when the Wright Brothers first flew a powered aircraft, aviation has not only exploded in popularity, but also has faced many challenges. Unfortunately, as the popularity of air travel increases so too does the risk of property loss and fatalities resulting from aviation accidents. Since the late 1960's the National Transportation Safety Board (NTSB) has maintained a database of all aviation accidents, including their causes. When investigating these accidents, icing was one of the primary meteorological factors the NTSB considered (Petty et al., 2003).

Aircraft icing has been recognized as a significant aviation hazard since before 1930 (Mack, 1998) when airplane manufacturers first tried to install mechanical devices designed for in-flight deicing. By 1981, the FAA had published a report entitled "Aircraft Icing Avoidance and Procedures" and airplane manufacturers were successfully installing mechanical devices designed for in-flight deicing. Despite these efforts icing still remains a problem today (Petty *et al.*, 2003). Again in 1997, in response to a demand from the White House Commission on Aviation Safety and Security, the FAA instated an In-flight Aircraft Icing Plan (AIRSI, 1999) to significantly increase the level of safety for aircraft (Reehorst and Politovich, 2003). However, even with these precautions, in the 19 years between 1982 and 2000 there were almost 700 lives and over 450 planes lost in general aviation accidents where icing played some role (Petty *et al.*, 2003). In the United States alone, an average of 24 accidents, 30 fatalities and 96 million dollars in damage result from icing related accidents each year (Paull and Hagy, 1999). Because of these disturbing statistics, pilots, engineers, air traffic controllers and meteorologists continue to work towards the prevention of aircraft icing.

This study aims to minimize icing dangers by creating a real-time, accurate, automated system that uses radar data and precipitation physics to reduce or even prevent aviation accidents related to icing. Before any details are given on how such a system could be created, a cursory review of some of the past work done in this field and a brief overview of some of the microphysical processes involved in the formation of icing conditions will be presented.

1.2 Review of Icing Research

Forecasting icing has been a goal of scientists since icing was first suggested as a possible cause for an airplane accident. Military aircrafts, especially rotorcraft, flying primarily at low altitudes from non-traditional airfields are particularly vulnerable to in-flight and pre-flight icing (Ryerson *et al.*, 2003). Thus during the Second World War, the military pushed icing research because the nature of army aviation puts their aircraft especially at risk. In fact, the first research project assigned to the Ames Aeronautical Laboratory in 1941, Research Authorization No. A-1, covered a study of means for protecting airplanes from the hazards of icing (Hartman, 1970).

In the past 10 years, advances in remote sensing technology, computers, and understanding of the microphysical processes have exponentially expanded the work done in this field. Field projects like AES/IAR in 1995, 1996, and 1997, NASA-Glenn/NCAR in 1994, 1996, 1997, and 1998, the Canadian Freezing Drizzle Experiment in 1995,1996,and 1997, Winter Icing and Storms Project winters of 1989-90, 1992-93, 1994-95, and 1997-1998, and AIRS in 1999-00, 2002-03, and 2003-04 added invaluable data and opportunities for coordinated joint research. Despite the considerable attempts that have been made to forecast icing there is still significant research that remains to be done (Hallett et al., 2002).

The oldest icing algorithms were developed in the 1940's and 1950's and used a few simple rules to forecast icing areas. The algorithms generally looked for regions of rising air with temperatures between 0 and -20°C. In addition a heavy emphasis was placed on synoptic patterns, front recognition and cloud formations. The algorithms gave very general results from minimal input but they offered a solid foundation on which many successive algorithms have been built. (AIRS I, 1999)

Over time, icing algorithms have become increasingly more and more sophisticated. Estimates of variables including temperature and vertical velocity have been improved with more detailed microphysical parameters such as the liquid water (ice) content of rain and clouds. In addition current icing algorithms have access to data from a variety of radars, radiometers, lidars, satellites, in-situ measurement, and models. Experiments have shown that an effective method for diagnosing icing conditions uses a combination of sensor data and model output fields. Currently there is an alphabet soup of newly-designed integrated systems attempting to detect and forecast icing. Based on the fact that no one source of information can paint a complete picture, two groups of solutions have emerged: systems using a large scale theoretical approach and technology-based systems focused on the scale of an airport terminal (Isaac *et al.*, 2001).

The larger-scale systems provide both diagnostic and forecasting services, with data that originates primarily from satellites, model output, and pilot reports. The systems use logical regressions to combine of data from among other things numerical models, surface observations, satellites, and radars (Pocernich *et al.*, 2004). All of the large-scale systems are comprised of primarily the same components, but each is combined in a unique way to provide the best forecast for the targeted climatological region and end user. CIP (Current Icing Product) and FIP (Forecast Icing Product) are the newest operational US systems being developed by the Research Application Program (RAP) at the National Center for Atmospheric Research (NCAR). They provide a large-scale but frequent (20 minute) product based on observations from the surface, satellites, and radar, as well as pilot reports (PIREPs) and model data from the RUC-II (Pocernich *et al.*, 2004). WSDDM (Weather Support for De-Icing Decision Making), a US product, and ADWICE (Advanced Diagnosis and Warning System for Aircraft Icing Environments), a European product, both use a similar combination of model and observational data (Rasmussen, 2001, and Tafferner, 2003) and produce results less frequently. SIGMA (System of Icing Geographic Identification in Meteorology for Aviation) is a French system based on the same principles (Le Bot, 2003) and AVISA (Airport Vicinity Icing and Snow Advisor), a Canadian system that uses GOES satellite data, scanning radar and model data to provide large scale results, but hopes to eventually include the work being done in this study to add emphasis on the airport terminal area (Driedger, 2004).

While these large-scale systems offer some valuable information, the fact remains that most icing accidents happen around the terminal area. In addition, the large-scale systems provide conclusions of icing conditions based on model and satellite data. Unfortunately, the nature of these indirect conclusions means that the value of the icing data is only as good as the skill of the models and the skill with which cloud data can be extracted from satellite data. Since neither source of data is perfect the output has a clear disadvantage. Moreover, these large-scale systems operate primarily at the same range as the official U.S.

forecasts, Airman's Meteorological Bulletins, and AIRMETs, all of which tend to cover broad areas and long (6 h) time scales (Hallett et al., 2002).

As a result of the limitations mentioned above and the high probability of an icing accident to occur near an airport, other researchers are focusing on a much smaller scale, limited usually to the terminal area of an airport. Systems built on this general principle are being developed by NOAA, NCAR, NASA GRC, MSC and others. They are more dependent on technology such as radar, radiometers, and lidars. Some examples include NOAA's GRIDS (Ground-Based Remote Icing Detection System), which is based on dual polarization scanning Ka-band radar and radiometery (Reinking et al., 2001); NASA's NIRSS (NASA's Icing Remote Sensing System), which uses a vertically pointing radar, a multifrequency microwave radiometer, and a ceilometer (Reehorst and Politivich, 2003); and SPolKa, a more costly system developed by the NCAR, and partially funded by the FAA, that measures differential attenuation in liquid water with a dual polarization multiple wavelength radar (Hallett at al, 2002).

The disadvantages of small-scale approaches are specific to the kind of technology used. Methods which involve radar data at multiple wavelengths often have problems when particles grow to approximately the same size as one of the radar wavelengths, and the usual Rayleigh scattering is replaced by Mie scattering. Radiometers have problems whenever they are wet, which unfortunately is not uncommon in icing situations, since much of the time interesting icing conditions are occurring aloft, there is rain falling at the surface. Finally, all technology based systems are costly and many of the systems which use only scattering or propagation based approaches encounter problems when identifying icing.

The rest of this study will address a unique approach to answer the icing question: an automated system that uses meteorological theory and data from a vertically pointing radar to provide real time diagnosis of icing in the vicinity of an airport. The idea behind this simplistic approach to icing stems from the advantage of both the large-scale (meteorological theory) and small-scale (technology) systems. Considering the fact that 95% of all icing accidents take place in the approach, landing, holding, or go around phase of flight (AIRS1 1999), this study focuses its resources where problems most often occur. However, unlike some of the other technological solutions, it does not rely only on technology to identify icing regions; rather the study used information from the VPR combined with the overall meteorological theory. Thus, the next sections will a lay out a brief overview of some of the microphysical processes involved in the formation of icing conditions.

1.3 Icing and Supercooled Liquid

Aircraft icing is a direct result of the co-location of supercooled liquid water (SLW) and an aircraft in the atmosphere. In 1975 the US Federal Aviation Administration concluded that only two factors are needed for an aircraft to experience icing: the temperature must be below zero and water must be visible as rain or cloud droplets (Sand et al., 1984). Today scientists understand that icing is related to both meteorological factors (temperature, liquid water content, and drop size distribution) and non-meteorological factors (speed of plane, angle of attack, and flap setting), but can only occur when SLW is present (Reehorst et al., 2000). SLW is defined by the American Meteorological Society Glossary as "Liquid water at a temperature below the freezing point" (Glickman, 2000). While most people have experienced SLW in the form of freezing rain, many do not realize how common the existence of SLW is in the atmosphere.

1.3.1 Where Does SLW Come From?

The primary source of water in the atmosphere comes from evaporation generated at the surface. Once the vapor is in the atmosphere, it can change state given favorable atmospheric and thermodynamic conditions. The vapor can change state to liquid (condensation), to solid (deposition). Saturation is achieved either by cooling the temperature of an air mass or increasing the amount of water vapor in an air mass.

At temperatures below zero, saturation with respect to ice will occur before (at lower vapor pressures) saturation with respect to water. Like water, ice can form by heterogeneous nucleation. However, unlike water, the number of particles available for heterogeneous nucleation is limited. In fact, there are about one million times less ice nuclei than condensation nuclei (Rogers and Yau, 1996). According to Fletcher (1962), a typical concentration of ice nuclei at -10°C is less than one nucleus per 100 liters. The concentration of ice nuclei increases to one active ice nuclei per liter at -20°C and continues to increase by a factor of 10 for each additional 4 degrees of cooling. Because of this dependence on temperature there are often not enough ice nuclei for heterogeneous nucleation to consume the available supersaturated vapor. If there is not enough energy to overcome the free energy barrier of crystallization and there are not enough ice nuclei or ice crystals, then the relative humidity will keep increasing and eventually saturation with respect to water will occur.

As long as the relative humidity is greater than 100%, water droplets will form and continue to grow. This can happen either because ice crystals are not present or because there is an updraft that provides moisture faster than the ice can absorb it up (Zawadzki et al., 2000). Because of the lack of ice nuclei, there is often liquid in the atmosphere at temperatures below 0°C (Korolev et al., 2004). Such liquid water is referred to as SLW (Supercooled Liquid Water).

SLW can also form when frozen ice crystals or snowflakes melt as they fall into a warm layer, becoming super-cooled in a colder layer near the surface. This explanation was traditionally thought to explain most occurrences of freezing precipitation; however, it appears that a considerable fraction of supercooled liquid is formed in temperatures entirely below freezing by the warm rain process. Studies conducted in the Canadian Maritimes found that more than 50% of freezing drizzle is formed entirely at temperatures below 0°C (AIRSI, 1999). Another study conducted in Maniwaki, Quebec (northwest of the AIRS study area) found that 38% of freezing precipitation forms through non-classical mechanisms (Strapp et al., 1996 and Cortinas et al., 2004).

1.3.2 Where Does SLW Pose the Greatest Danger?

It is clear that SLW is not at all unusual in the atmosphere. Geographically, the areas with the greatest risk for icing are cold and moist environments. Prime areas for icing concern are the Great Lakes region of the United States and Canada and the Canadian Maritimes. A climatology of North American reveals that there is a maximum occurrence of freezing precipitation over Newfoundland (about 150 h/year) and near the Great Lakes (about 75 h/year) (Strapp et al., 1996; Stuart and Isaac, 1999). A more recent study of freezing precipitation (Cortinas et al., 2004) also shows a maximum in freezing rain and freezing drizzle in Quebec Canada. When considering climatology in combination with aircraft traffic, the Great Lakes area becomes the region most in danger of having an icing related aviation accident.

SLW is also limited to specific regions of a vertical column. In air masses with cloud top temperatures of -10°C or higher, the probability of finding an entire cloud of SLW drops is more than 40%. Even at a cloud top temperature of -20°C the probability of finding an entire cloud of SLW is on the order of 10%

(Pruppacher and Klett 1997). It follows that the majority of icing events occur at temperatures warmer than -10°C and it is clear that SLW is most often a concern in the lower atmosphere (Isaac et al., 2001a). Extending that logic one step further, it is easy to see that for commercial aircraft, which usually travel above 30,000 feet, the take-off and landing is the most dangerous part of the trip. Thus, it is no surprise that an analysis of 39 accidents resulting from in-flight aircraft icing showed that 37 of those accidents (95 %) took place during the approach, landing, holding or go-around phase of flight (Air Line Pilots Association (Hallett et al., 2002). A larger study done by Green (2003) found that out of 120 military aircraft incidents 90% of icing problems occurred during these same phases of flight. In the hopes of reducing the icing hazard to aircraft just where the threat is highest, this study uses the physical characteristics of SLW, to provide a real-time icing detection/warning system for airports.

1.4 The VPR

The VPR is a vertically pointing X-band radar, developed at McGill University that measures reflectivity and Doppler velocity in a column above the radar itself. The VPR is based on a boat radar transmitter-receiver with a parabolic antenna and connected to locally developed data collection system. The VPR is designed to measures those echoes which pass above it, in high resolution spatially and temporally.

The VPR was used as early as the 1950s. In 1974 Weisse and Hobbs (1974) used it to study cloud physics including the growth of ice crystals through riming in regions of supercooled liquid. While the X-band VPR has not caught on for operational use, it continues to be a valuable research tool. The main advantage of the vertical pointing radar is its ability to act as a rain or snow gauge, measuring the amount of precipitation located in a vertical column above the radar.

In the past VPRs have been used extensively to study the bright band (Fabry and Zawadzki, 1995; Austin and Bémis, 1950), attenuation (Bellon, et al. 1997), and other cloud physics issues like snow trails and generating cells (Xue 1999; Marshall 1953). Recently the focus has been on using the VPR for icing (Večei 2002; Côté 2002; Zawadzki and Fabry 2000A; Zawadzki and Fabry 2000B; Bell 2000) and to this end the VPR has been deployed at several recent field projects including AIRS I and AIRS II.

1.5 Outline and Thesis Objectives

The general objective of this study is to describe a method for identifying regions of SLW with a VPR. Specifically, the study will progress in the following way:

1. Chapter 2: Describe the research approach, including the goals, the design, the AIRS II field project in which this study is framed, and the data used;
2. Chapter 3: Develop five fuzzy logic algorithms used to identify the bright band, as well as regions of snow, rain, rime, and drizzle;
3. Chapter 4: Apply three further algorithms to (1) identify modes in the distribution of fall speed, thus separating out the elements of mixed precipitation, (2) calculate the LWC with the snow flux algorithm, and (3) calculate the LWC with the snow density algorithms;
4. Chapter 5: Combine all the algorithms into one system and present 3 case studies with all possible verifications.

A discussion of these goals and the future of this research will follow.

Chapter 2

Project Goals and Design

2.1 Goals

As stated, the goal of this project is to create elements for an operationally valuable system to detect SLW and other dangerous icing conditions in the airport terminal area. The automated system uses Doppler spectrum, fall velocity, and reflectivity data from a VPR to run a series of classification algorithms based on proven precipitation physics. Given the results of the classification algorithms, two quantitative algorithms based on the flux and density of hydrometeors can be applied to regions of frozen precipitation to calculate the LWC and provide a real-time diagnosis of icing in the vicinity of an airport. The outline of this project is expressed in a flow chart in figure 2.1.

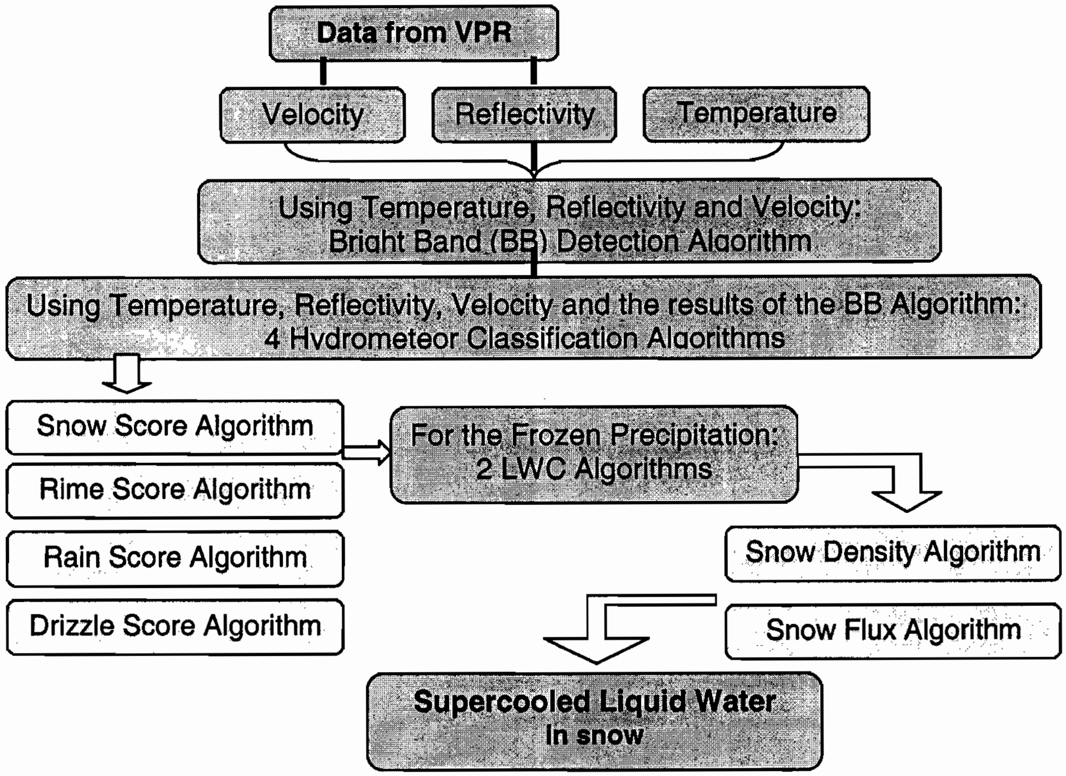

Figure 2.1: Flow chat for project. Temperature is the only data that is not directly from the VPR and in the end the amount of SLW provides information on the icing danger.

In order to successfully identify icing conditions, there are five main combinations of hydrometeors that must be recognized: 1) liquid cloud with no drizzle and no ice, 2) liquid cloud with drizzle and no ice, 3) liquid cloud hidden in snow or ice cloud, 4) liquid cloud and drizzle hidden in snow or ice cloud, 5) freezing drizzle or rain (Fabry et al., 2001). Detecting the precipitation, identifying any mixed precipitation, and quantifying the amount of LWC are the main challenges put to any icing system. Separating individual types of hydrometeors, such as snow and drizzle or rain and rimed snow, is the key to identifying icing regions; however, it is not possible with many types of icing detection systems. The advantage of the VPR-based remote sensing technique is the availability of fall velocities, which provide information about the type, makeup, and even the surroundings of a particle. With the help of these fall velocities, the VPR is able to distinguish between different types of hydrometeors and overcome many of the challenges facing other icing systems.

2.2 Project Design

To identify regions of SLW, a series of algorithms have been created, built upon one another, and incorporated into a single system. All the algorithms use data primarily from the VPR, although when available, vertical temperature profiles are incorporated to add value to the algorithms. Individual classification algorithms were created to automatically identify any melting layer, and regions of rain, snow, rime, or drizzle. These algorithms use fuzzy logic and binary logic approaches to match the data with expected characteristics of rain, snow, drizzle, and rime. Another algorithm was designed to distinguish modes, or peaks in the distributions of fall velocities, where each peak may represent a different type of precipitation. Next, algorithms used to quantify LWC based on the mass flux and density of snow were adapted and applied where appropriate. Finally, all the algorithms were combined into one system. By keeping the project goals simple, using limited inputs from a relatively inexpensive, stand alone technology and sound meteorological theory governing the growth and distribution of particles, this study keeps the potential costs low and the potential benefits high.

2.3 Alliance Icing Research Study I and II

A field project named the Alliance Icing Research Study (AIRS) was held at Mirabel Airport, just northwest of Montreal in 1999-2000 (AIRS I), 2002-2003 (AIRS 1.5), and in 2003-2004 (AIRS II). Mirabel was chosen as the location for AIRS based on its climatology, affordability, and its proximity to both useful meteorological equipment and high aviation traffic. The AIRS experiment was a truly international effort with over 33 scientists from 17 different organizations, including participants like FAA, GRC, MSC, NASA, NCAR, NOAA, TC, and McGill University (Hallett et al., 2002).

The AIRS II experiment had eight goals, four scientific and four operational. The four main scientific goals were: 1) The investigation of micro-, meso-, and synoptic-scale conditions associated with supercooled large drop formation; 2) The detection of the conditions needed for cloud glaciation (transition of clouds from liquid to ice); 3) The study of the distribution of ice crystals and SLW and the environment where they can co-exist; and 4) The response of remote sensors to clouds composed of various types and concentrations of ice crystals and liquid drops, so as to remotely determine cloud composition. The four main operational goals were: 1) Testing and evaluating systems for detection, diagnosis, and forecasting of winter weather hazards, with an emphasis on in-flight icing; 2) Improving aircraft icing forecasts; 3) Better characterizing the aircraft icing environment; and 4) Better characterizing the accretion of ice and aerodynamic performance of an aircraft in an icing environment (Hallett et al., 2002). This VPR project described in this paper fits nicely into the goals established by the AIRS organizers, especially the first and second operational goals.

2.4 VPR Data from AIRS

During all the AIRS experiments the VPR was located at Mirabel, and collected data throughout the entire experiment period. The VPR has a 3.2 cm wavelength and a pulse repetition frequency of 671 Hz. Its Nyquist velocity ranges from -5.2 m/s to 5.2 m/s, but for this project was shifted to a range of -8.4m/s to 2m/s (with negative values traveling towards the ground).

The VPR is an ideal instrument to study precipitation echoes at all altitudes in high resolution. The radar provides information at 2 s resolution over the horizontal and 37.5 m resolution in the vertical. Because of the simplicity that only one elevation angle (90°) offers, the radar is able to provide detailed images of the weather directly above it. The VPR can detect all precipitation targets, in addition to birds, bugs, ice clouds, and clear air echoes associated with turbulence in developing cumulus clouds. An example of VPR data can be seen in Fig. 2.1 and the details of the radar follow in Fig. 2.2.

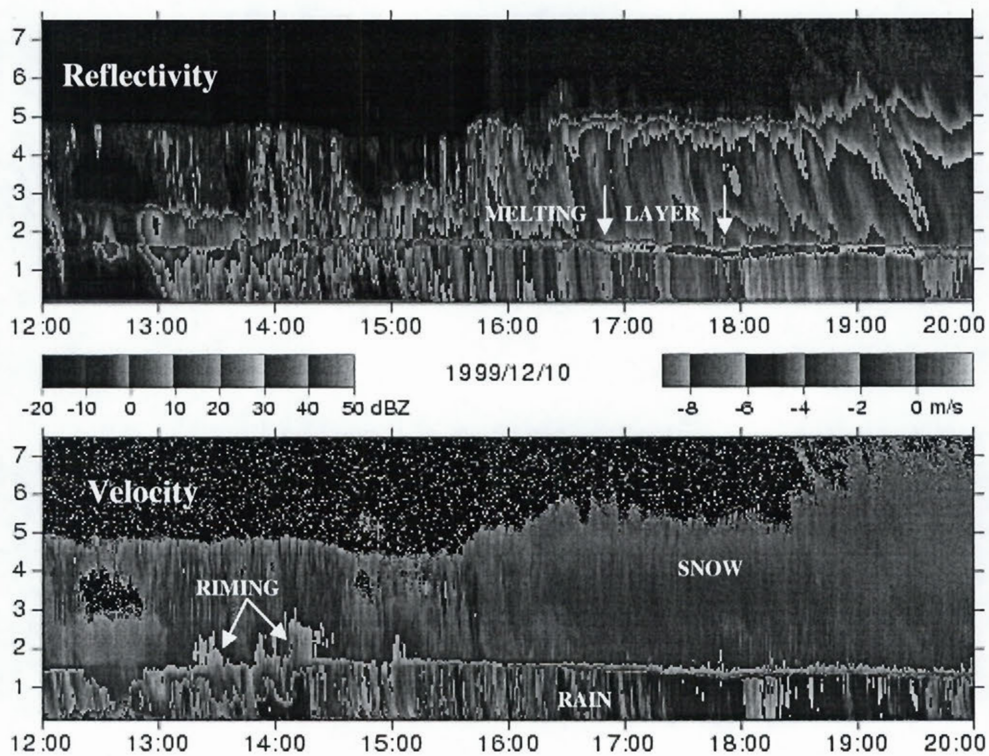

Figure 2.2: Time-height section of radar reflectivity (top) and vertical velocity (bottom) in precipitation. In this example, one can observe a variety of types of precipitation including snow, rain, and rime. Furthermore, the presence of some of these observed hydrometeors such as rimed snow imply the presence of invisible liquid clouds. At 2 km, between 1700 and 1930, a bright band indicates snow clearly melting into rain.

Wavelength	3.2cm
Pulse Repetition Frequency	650Hz
Peak power	25kW
Dish Diameter	1.2m
Minimum height	75m
Maximum height	9000m
Pulses averaged	1200
Pulse length	1μs
Bin Size	37.5m

Table 2.3: McGill VPR details (Adapted from Côté, 2002 and Večei, 2002)

The variables collected by the VPR are reflectivity (Z), Doppler velocity (v), and power spectra. Reflectivity is a measure of the amount of power returned to the radar after bouncing off of a target. Reflectivity is generally expressed in dBZ (a log scale) because of the broad range of reflectivity values experienced at one time. Reflectivity as seen in (2.1) is dependent on the diameter of the particle size to the sixth power.

$$Z = \sum_{v} D^6 = \int_0^\infty N(D)D^6 dD \tag{2.1}$$

The Doppler velocity measures how fast targets fall, based on a principle developed in 1853 that calculates speed from frequency changes in the returned signal (Rinehart, 1997). Since the VPR points vertically, Doppler velocities correspond to vertical velocities. Finally, the 128-bin power spectrum provides a power returned at each fall velocity within the radar's Nyquist frequency.

During AIRS, the data were collected in a very standard way regardless of weather conditions: minimum height of data collection was 75m and the maximum was 9000m. Horizontally, the data was collected in 2 second and 37.5m resolution for reflectivity and velocity and 30 s resolution for the 128-bin power spectra. To synchronize with the spectra data, the velocity and reflectivity data was averaged over 30 seconds. Then to minimize for trails, streaky structures in snow caused by horizontal winds (Douglas et al., 1957), all the data was averaged to 10 minutes. Therefore, for every 10 minute, period the data was analyzed at 78 heights, where each height contains a record of the velocity, reflectivity, a correction factor, and the 128-bin power spectra. An example of power spectra follows in Figure 2.3:

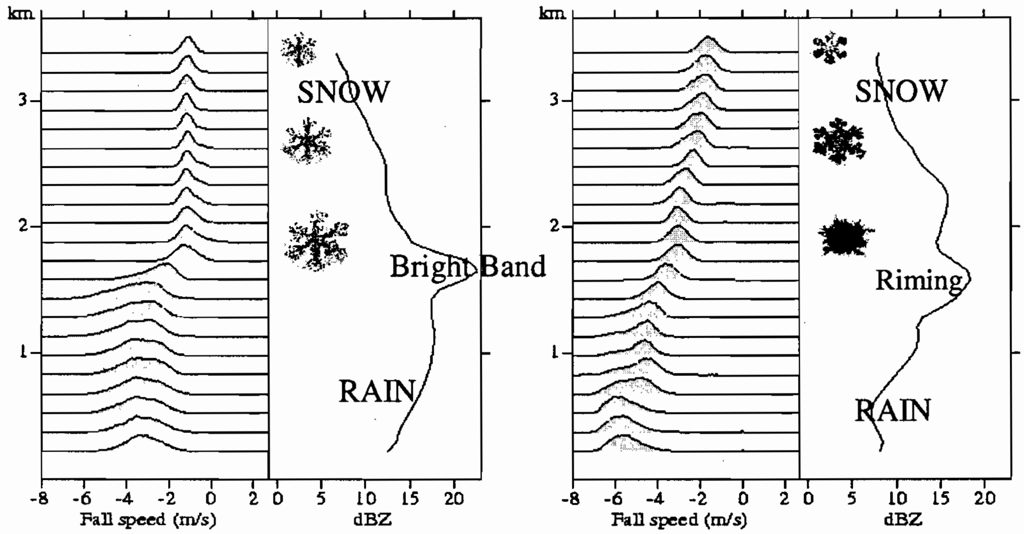

Figure 2.4: Spectral data from the VPR. The spectra on the left show snow, followed by rain with a strong bright band between. The spectra on the right show snow followed by riming. (Fabry et al 2003)

Before any further calculations were made, the raw data were modified from their original form in order to correct for attenuation, noise, and changes in air density. In addition, the 128-bin power spectra were converted into the same units as reflectivity. Attenuation can occur on the radome or along the path. During winter storms, the attenuation at X-band is relatively small, both along the path and on the radome. Of the two, a wet radome is associated with the most attenuation and thus a systematic correction factor was applied to the data. Correcting for noise allows the real radar signal to be cleanly resolved from noise. The signal-to-noise correction factor is unique to each time and height, and when applied to the raw data in (2.1) it acts to remove the noise floor. If the signal-to-noise ratio was less than -8 dB, then the signal was considered indistinguishable from the noise. In other words, there were no targets in those regions to give valid data. Otherwise, the correction factor was applied to reflectivity in the following way:

$$\text{Corrected reflectivity} = \text{reflectivity} * \frac{\text{correction factor}}{1 + \text{correction factor}}. \qquad (2.2)$$

Next, the velocity values were corrected (Kessler, 1969) for the air density in the following way:

$$\text{Corrected Velocity} = \frac{\text{velocity}}{e^{0.000048 * \text{height(m)}}}. \qquad (2.3)$$

This equation corrects the fact that the same particle will fall faster higher in the atmosphere than it would at lower altitudes, since the atmosphere is denser near the earth's surface.

Finally, the 128-bin power data was converted to reflectivity for ease of understanding and comparison. Power was converted to reflectivity by dividing the given power by the radar correction factor and the $\|K^2\|$ value, which is always equal to the $\|K^2\|$ value of rain as a result of the way the data was calculated. The equation to make this calculation follows:

$$\overline{P}_r = C_{radar} \left\|K^2\right\| Z \quad \Rightarrow \quad Z = \frac{\overline{P}_r}{C_{radar}\left\|K^2\right\|} \qquad (2.4)$$

It is important to remember that the radar constant C_{radar} changed for each height and time. Accordingly, the C_{radar} was first calculated at each height and time by dividing the sum of all 128 power bins by the uncorrected reflectivity for each height. Then, with the new correction factor for each height, all 128 individual power bins were transformed into linear reflectivity values.

2.5 Case Studies

While the goal of this study is to develop a system that runs continuously, the presented calculations and verifications were made primarily from three days: December 10th 1999, December 13th 1999, and December 16th, 1999. These days were chosen for the challenges they presented and for the availability of radiometer or aircraft data for verifications. All the case studies included some drizzle, rain, snow, riming and possibility of SLW. If the algorithms perform well on the challenging days, extending the system to run continuously should not be a problem.

Chapter 3

Classification Algorithms

3.1 Fuzzy Logic Algorithms

In this chapter, a series of classification algorithms are created using fuzzy logic to identify different types of precipitation. All the algorithms use the reflectivity, velocity and temperature data available, and can be applied either to the data as a whole or to the separated modes (described in Chapter 4).

3.2 Bright Band Algorithm

The bright band has been studied since the beginning of radar meteorology (Marshall et al., 1947, Cunninghan, 1947, and Fabry and Zawadzki, 1995) and is still a very useful way of finding the melting layer today. In this study, finding the bright band was the first step in teaching the computer to examine radar data the way a meteorologist examines a radar image. To the human eye, the bright band stands out as a bright horizontal line, and is one of the most obvious features on a radar image. Once this line has been identified, a meteorologist can assume that the area above the bright band is dominated by frozen precipitation and the area below the bright band is rain. Teaching the computer to do what is second nature to humans is difficult. The task involves understanding the meteorological theory behind the bright band, understanding the logic that both humans and computers use to make decisions, and judging the relative importance of each of the available resources.

3.2.1 What is the Bright Band?

The bright band is the name given to the level of melting snow/ice as seen on a radar image. This layer is also known as the melting layer, but melting by itself is not a sufficient condition for a bright band signature (Fabry and Zawadzki, 1995). The AMS glossary defines the melting layer as "the altitude interval throughout which ice-phase precipitation melts as it descends" (Glickman, 2000). The temperature in this layer is usually slightly warmer than 0°C, and the thickness of this layer is determined both by the amount of time sufficient for all the particles to melt and the fall velocity of snow. On average, the bright band is usually a few hundred meters thick and its top is centered 100m below the 0°C isotherm. However in cases where the fall speed of the melted and the frozen particles are similar there may be no bright band at all. (Fabry et al., 2003) The term bright band comes from the fact that the reflectivity in this layer is usually very high, thus it appears bright on a radar image.

The physics behind the increased reflectivity that causes a bright band are quite easy to understand. When frozen particles cross the 0°C level, they begin to melt, slowly turning to liquid, and eventually collapse into comparatively smaller raindrops. By modifying (2.3) one can see that power returned is simply reflectivity, divided by the square of the range to the target, multiplied by the radar constant and the $||K^2||$ value.

$$\overline{P_r} = C_{radar} \|K\|^2 \frac{Z}{r^2} \tag{3.1}$$

The dielectric factor (or $||K^2||$) value is the main reason that reflectivity changes in response to melting: $||K^2||$ for liquid is 0.93, $||K^2||$ for ice is 0.21, and $||K^2||$ for the air-ice mixture that makes up snow is even lower than 0.21 (Rogers and Yau, 1996). During melting, a film of water forms over the particle's surface, and the $||K^2||$ value increases towards 0.93, despite the fact that the particle still has the shape of a snowflake. As the particle continues to melt, it collapses into a raindrop, dramatically decreasing in size. Since Z is dependent on diameter to the 6^{th} power, any increase in power from the change in $\|K^2\|$ is soon lost by the decrease in size. In addition, since rain falls much faster than snow there is a decrease in the number of precipitation particles per unit volume, equivalently a decrease in the concentration that the radar can see. Thus the bright band is a narrow layer of high reflectivities because of the increase in the $\|K^2\|$ and the subsequent decrease in particle size and concentration.

3.2.2 Fuzzy Logic

Most computer programs make decisions using a binary 0 or 1, yes or no, structure. In reality, problems are rarely simple enough for people to make decisions in such a black and white manner. To improve the computer's decision making ability, this project uses fuzzy logic to provide a more subtle, or human, way of making decisions for several important algorithms.

Fuzzy logic was introduced by Zadeh (1965) as fuzzy set theory. Over time, this idea developed into fuzzy logic, which enables the processing of imprecise information by means of membership functions. More conventional Boolean characteristic mappings use only two values: one, when an element belongs to the set; and zero, when it does not. In fuzzy set theory, an element can belong to a fuzzy set with its membership degree ranging from zero to one.

Fuzzy logic is often confused with probability theory. However, unlike probability theory that describes the likelihood that something is true, fuzzy logic determines the degree to which something is true. In this way, it allows a user some grey area between black and white. Like humans, but unlike binary logic, fuzzy logic is extremely good at making conclusions based upon incomplete, imprecise, vague, ambiguous, or noisy data.

Fuzzy logic uses a rules-based system, adapted by the end-user to best fit a given situation. Each problem must be broken down into a group of factors. Then, each factor has a 'yes' point, where the score is 1, a 'no' point, where the score is 0, and a system to assign scores in between the yes and no points. Finally, depending on the user, a set of rules is created to combine the scores from each factor into a final decision.

3.2.3 Fuzzy Logic, Data, and Algorithm Rules

In the case of the bright band, fuzzy logic can answer the question: is there a bright band, and if so, where is it? To answer this question with fuzzy logic, the problem must be broken down into a set of criteria that affect the location of the bright band: temperature, reflectivity, and velocity. Rules are assigned to determine the score for each factor, and a set of rules must be established to combine the scores of each of the factors into a total score for the bright band.

3.2.3.1 Factors

Six parameters may influence to the bright band: (1) change in the dielectric constant through melting, (2) change in fall velocity throughout melting, (3) precipitation growth, (4) change in particle size distribution, (5) change in shape or orientation effects, and (6) the distribution of water in a melting snowflake (Fabry and Zawadzki, 1995). In terms of what can be observed by radar, these will be simplified into temperature (1), derivative of velocity (2), and reflectivity score (3-6).

For the bright band, the fuzzy logic criteria are temperature, derivative of velocity (Dvelocity), and the presence of a local maximum in Z (Rscore). Temperature can be derived from sounding data or model data and must be interpolated to have the same time and height as the radar data. This study uses sounding data, which was available as a result of the AIRS field project. In many other circumstances the result would be better with model data that has better time and space resolution. The peak of the derivative of velocity (the change in velocity with height) shows the area where the particles collapse from snowflakes into raindrops and begin to fall quickly. The vertical velocities observed by the VPR are very close to the true fall velocity of the represented particles in stratiform precipitation; however, updrafts and downdrafts do affect the observed vertical velocities. In convective conditions observed fall velocities can not be taken as fall velocities. In stratiform conditions, time averaging helps to minimize the effects of updrafts and downdrafts and provides approximately true fall velocities. Reflectivity score (Rscore) is calculated in (3.2) by taking each reflectivity value and subtracting the average of the points 150m above and below it.

$$\mathrm{Rscore(h)} = \mathrm{dBZ(h)} - \frac{(\mathrm{dBZ(h+150m)} + \mathrm{dBZ(h-150m)})}{2} \tag{3.2}$$

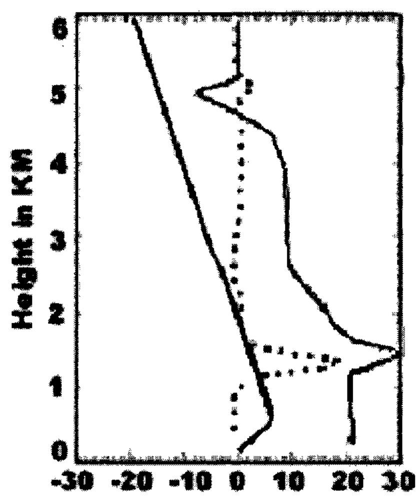

Figure 3.1: Rscore is calculated by subtracting the average of the reflectivity 150m above (yellow) and 150m below (blue) points from each reflectivity (red) point. Graph of temperature▬, derivative of velocity ...... and reflectivity____.

3.2.3.2 Rules

The rules for each factor in the bright band algorithm are fairly simple, and are based on the physics of the melting layer. Each factor has a cutoff point where no bright band is possible, and a score of zero is assigned, as well as a point where conditions are ideal for the formation of a bright band, and a score of one is given. The specific limits for temperature, Rscore, and Dvelocity are explained in the following three paragraphs respectively. In all cases, there is a simple linear distribution between the cutoff point and 100% point. These distributions are shown in Fig. 3.2. Finally, the rules for combining each criterion into an algorithm are explained.

Figure 3.2: Rules for bright band detection by fuzzy logic. These three graphs show the fuzzy cutoff points for the bright band algorithm. Ideal conditions for the bright band occur when temperature is between 0-2°C, Rscore is greater than 6.5dB and Dvelocity is greater than 4m/s per 150 m.

For temperature, the cutoff points are -6°C and 6°C, and the 100% points are between 0°C and 2°C. The cutoff boundaries were chosen as the temperature where melting just begins and the level where melting must be finished. A temperature of -6°C corresponds to about 1200 meters above the bright band, a region where reflectivity has been observed to increase. This reflectivity increase is due to an increase in particle growth by aggregation. The peak area of the bright band is usually on the warm side of the zero degree isotherm, so the 100% fuzzy logic score was limited to the region 0°C to 2°C. (Stewart et al., 1984, D'Amico et al., 2000) In 1947, Cunningham (1947) predicted that the peak return in radar reflectivity would be below the 0°C isotherm, at the level where a large portion of the particle is liquid water, but the size of the particle and number of particles per volume is still reflective of snow. Much more recently, Stewart found this peak level of the bright band to be at about 2°C (Stewart et al., 1984). The lower boundary of the bright band is more difficult to determine exactly. Snow particles have been sighted in very dry air at temperatures as high as 10°C (Ahrens, 2000), but generally it is safe to assume that by the time the temperature reaches 6°C, all the particles have melted.

For reflectivity, the cutoff point was chosen as a 0 dB local maximum over 300 meters and the 100% point was chosen as a 6.5 dB local maximum over 300 meters. Any maximum greater than 6.5 dB was assigned a score of 1, in part because this limit is often quoted as the value simply resulting from to a change in the $||K^2||$ value and in part because 6.5 dB was observed frequently in case studies of the bright band (Fabry and Szyrmer, 1999). There are many factors which can affect this criterion, including the width of the bright band, particle size distribution, particle concentration, shape and orientation affects (Fabry and Zawadzki, 1995) and density. Of these five factors, the biggest effects are caused by particle density. Density changes are most often associated with riming and by extension, SLW, so these changes are key to identifying icing regions. Furthermore changes in density affect the fall speed of particles, whereby denser particles fall faster. Because the width of the bright band is determined by the difference in fall speed between the frozen and melted particles, riming or increased density can lead to small value of Rscore, thus even through there is melting there will be no bright band signature.

For the derivative of velocity, the cutoff point was chosen as 0 and the 100% point was chosen as the change of more than 4m/s over 150m or over any three velocity points. The fall velocity of particles does not change greatly in a homogenous environment, so it is an excellent criterion to use when selecting the bright band. The only challenge here was choosing the 100% cutoff value. In this case, a value of 4m/s over 150m was chosen to represent the difference in the average observed fall velocity between rain (6-8 m/s) and snow (1-2m/s) (Drummond et al., 1996).

Having established rules for each factor, the factors were combined with another set of rules. Based on the quality of the data the criteria were weighted. Temperature was only given a 20% weight because the data was less accurate and the range of temperatures where a bright band could be found was large. Reflectivity was also weighted less with only 30% because it is affected by particle size and many other factors. For these reason velocity is weighted at 50%, while reflectivity and temperature are weighted correspondingly less.

The level at which the velocity and reflectivity score are calculated are different because of the physics behind a change in reflectivity and velocity in the melting layer. Reflectivity increases during the first stage of melting, where aggregation sometimes occurs and the $||K^2||$ values increase. Velocity, on the other hand, increases during the final stages of melting due to increased fall speed. In other words, reflectivity changes when particles are still essentially frozen and behaving like a snowflake, but have a thin layer of water over their surface. Velocity changes the most when particles complete their melting into raindrops. The distance of 300 was used in the bright band algorithm because 300 meters represents the average width of a bright band (Fabry and Szyrmer, 1999). Figure 3.3 shows the graphic representation of the three individual factors followed by the algorithm's conclusion of where the bright band exists.

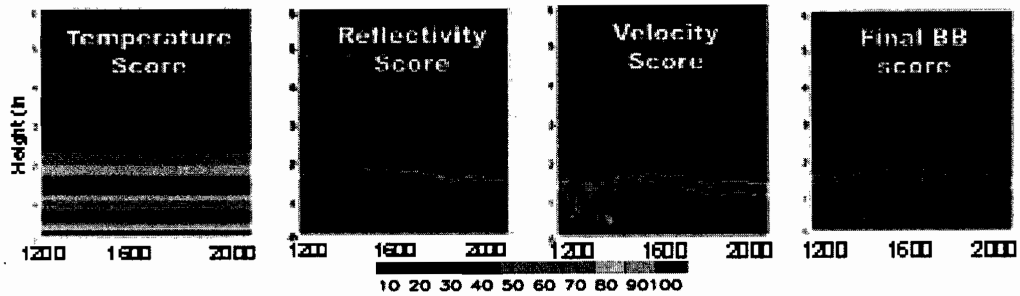

Figure 3.3: Scores for bright band detection by fuzzy logic. This figure shows the score for temperature, reflectivity, and velocity (from left to right). Red indicated a score of 1 and black a score of 0. The fuzzy logic algorithm calculates a bright band by combining these criteria with 20%, 50%, and 30% weights respectively; Velocity is taken 300m below both reflectivity and temperature. The green bright band on the right is a combination off all the areas that have a score of 50% or higher. When compared to the raw data in Fig. 2.1 the algorithm accurately represents the bright band.

3.2.4 Temperature

At this point, it is worth noting that the temperature data is the least reliable data used in the calculation of the bright bands (as well as in all the subsequently described algorithms). Temperature data comes from radiosonde soundings, which were released every 6 hours during interesting weather at the AIRS site. When available this data can then be interpolated to match the VPR data in height and in time. In cases where AIRS soundings were not available, other local soundings were used or the bright band algorithm was modified by weighting velocity to 60% and reflectivity to 40%.

Even when temperature data is available from sounding or model data is can not be blindly trusted. Many of the processes involves in icing, such as the riming of snowflakes, actually increases local temperatures due to the latent heat release. For these reasons temperature is given a lesser weight when used in all the algorithms.

3.3 Identifying Hydrometeors: Rainscore, Snowscore, Rimescore, and Drizzlescore

Once the presence and location of the bright band are established, the next step is to automatically identify precipitation types as viewed by the radar. Ideally there should be a simple zone with frozen precipitation above the bright band and liquid precipitation below it; however, reality is never so simple. The most interesting cases related to icing occur when SLW exists above the bright band. Fortunately each particle has an almost unique pair of velocity and reflectivity values which, when observed by a VPR, allows a computer to identify the type of precipitation. By merging data from the past several years, a picture of precipitation types for each velocity-reflectivity combination emerges (see Fig. 3.4).

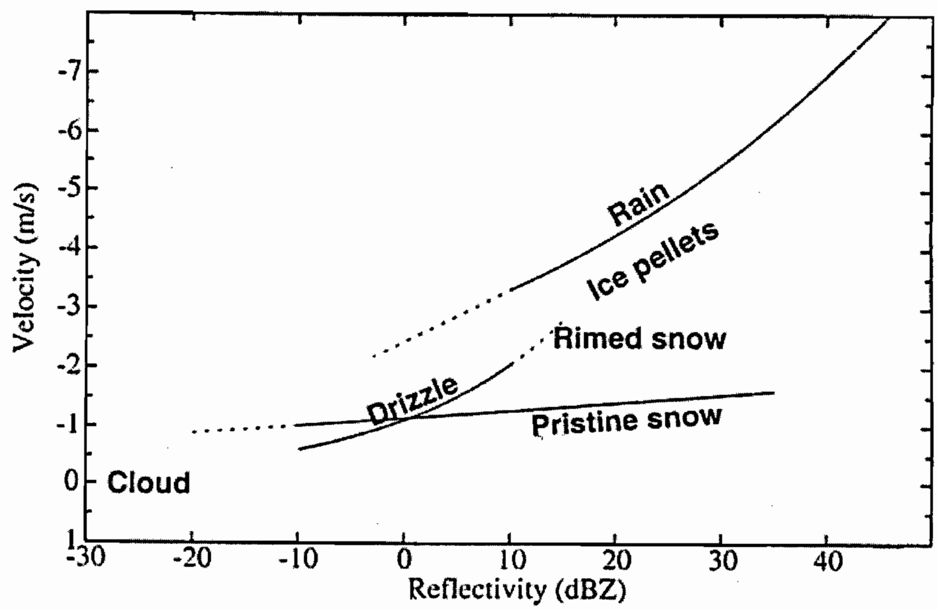

Figure 3.4: Reflectivity-Velocity pairs associated with different types of targets. (Côté, 2002 and Večei, 2002)

Some areas of the figure clearly depict one type of precipitation, such as the high velocity, high reflectivity areas of rain, and the low reflectivity, zero velocity areas of cloud. However, there are also areas of average reflectivity and average velocity which are typical of mixed precipitation and can be among other things a combination of snow, drizzle, rimed snow, or ice pellets. The following section will use radar observations and theory to describe the relationships between velocity and reflectivity for rain and snow, as well as the fuzzy logic rules used to calculate the snowscore, rainscore, rimescore, and drizzlescore algorithms.

3.3.1 Determining the Best ZV Relationship

Determining the relationship between velocity and reflectivity for all given types of targets (ZV relationship) is the first step in establishing fuzzy logic rules for hydrometer identification. Previous ZV relationships for rain have been described by Rogers (1964), Joss and Waldvogel (1970), Steiner (1991), and Sauvageot (1992). Snow exhibits a simpler relationship than rain since the velocity is about the same regardless of the reflectivity. Based on an assumption of the form of the size distribution given by Sekhon and Srivastava (1970), a relationship between V and Z can be determined. Sauvageot finds a ZV relationship for snow of:

$$V= 0.817Z^{0.063}. \tag{3.3}$$

The ZV relationship for rain is more difficult to calculate than the ZV relationship of snow because the fall velocity of rain is very dependent on its reflectivity. For rain, any increase in reflectivity usually corresponds to an increase in velocity, enticing Rogers, Joss and Waldvogel, and Steiner to develop a power law to find a ZV relationship. Rogers assumed no vertical air motions, a Marshall-Palmer (1984) drop size distribution, and a terminal velocity dependence on drop size given by a Spihaus (1984), and calculated a relationship of:

$$V=3.8Z^{0.072}. \tag{3.4}$$

Due to the large variability in the drop size distribution, which has more variability than the Marshall-Palmer distribution, Rogers' relationship is not entirely accurate. Joss and Waldvogel (1970) approached the problem with data rather than attempting to calculate the solution. Using a power law relationship, and data from England, Germany, and Panama, they found a relationship for rain of:

$$V=2.6Z^{0.107}. \tag{3.5}$$

Steiner (1990) used the same idea, fitting a power law relationship with data from Hoenggerberg in Zurich, Switzerland to determine a relationship of

$$V=2.95Z^{0.098}. \tag{3.6}$$

To test the validity of these relationships in the area of this study, each relationship was plotted over the POSS (Sheppard, 1990) precipitation data gathered at McGill. The data used includes over 10,000 minutes of rain with drops greater than .1mm (G.W. Lee, 2004, private communication). The POSS is a continuous wave bi-static X-band radar, and it offers a good way to test the average ZV relationship for rain. Plotting the POSS reflectivity and Doppler velocity for rain data on a log/log plot, with the average values highlighted in red, the Steiner relationship in blue, and the Joss and Waldvogel relationship in black, it is clear that the given relationship does not accurately reflect the observations in Montreal.

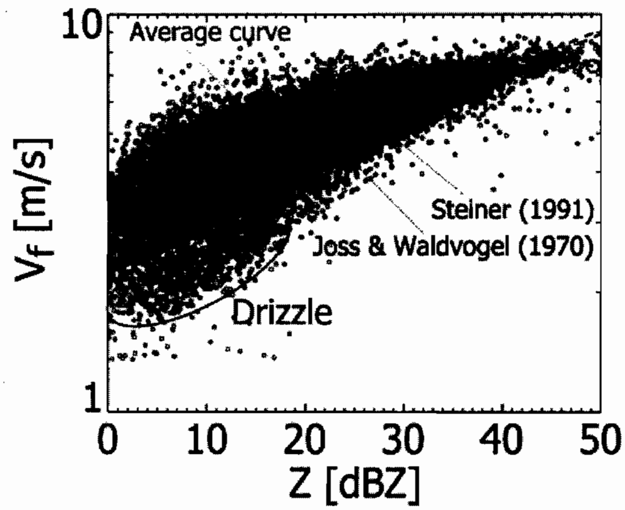

Figure 3.5: POSS data with over plotted ZV relationship (G.W. Lee, personal correspondence,2004)

The Rogers relationship, the first developed. is the least accurate and the worst fit. Joss and Waldvogel developed a slightly better fit and Steiner's fit appear to be quite close to the average; however, with all the POSS data available calculating a relationship unique to this area with local data is more desirable.

In an effort to calculate a new relationship the POSS data was re-plotted on a series of log/log, log/linear, linear/linear plots. The best representation of the data was a log/linear plot with linear velocity and log reflectivity. When displayed in this manner, the data appear to have more of a linear tendency, so several relationships were fit to the data.

$$\text{1st order } V=2.7+1.1\log_{10}(Z) \quad (3.7)$$

$$\text{2nd order } V=2.7+1.1\log_{10}(Z)-6.8*10^{-4}\log_{10}^{2}(Z) \quad (3.8)$$

$$\text{3rd order } V=2.9+.6\log_{10}(Z)+.03\log_{10}^{2}(Z)-4.6*10^{-4}\log_{10}^{3}(Z) \quad (3.9)$$

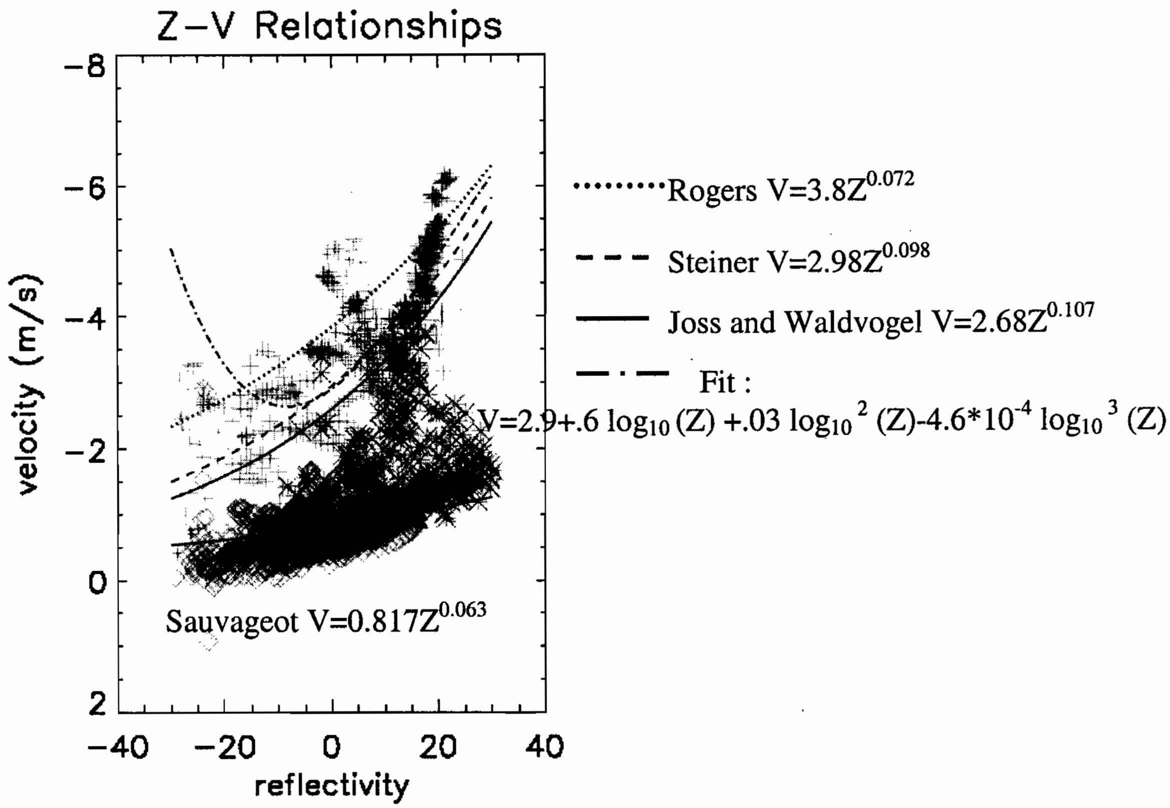

Figure 3.6: ZV Relationships plotted over data from 12/10/99. In this figure blue crosses represents rain below the bright band, while red diamonds are targets above the bright band and represent snow, The black stars represent the bright band. Sauvageot fit the data well for snow, and for rain both Steiner and the 3rd order fit do a good job. When using the 3rd order fit, cutoffs at -1.5 m/s and -4.5 m/s velocity is used to correct for the fact that the relationship is only valid at values greater than 0dBZ.

When compared to past data, the third order fit best represents the rain as seen in the observations over Quebec. The only problem with this relationship is that the POSS is less sensitive than the VPR. Thus, like the POSS, the relationship is only valid down to a reflectivity of 0 dBZ, while the VPR extends to reflectivities as low as -40dBZ. For reflectivities below 0 dBZ the third order fit gives erroneous results so constant limits of -1.5m/s and -4.5 m/s are used.

3.3.2 Fuzzy Logic Rules for Snowscore Algorithm

Given the ZV relationship for snow, a set of fuzzy logic rules must be established to determine the likelihood that a particle is pristine snow (unrimed). Thus, the snowscore algorithm follows the basic pattern established by the bright band algorithm. The factors for snowscore are temperature, reflectivity, and velocity. Velocity was given a score based on how much the velocity at any given reflectivity deviates from the idealized ZV relationship. Then, as with the bright band, a final set of rules was established to combine the scores from each factor.

3.3.2.1 Rules

The rules for each factor are fairly simple and are established in much the same way they were for the bright band. Each factor has a cutoff point where no snow is possible, and is given a score of zero, plus each factor has a point where conditions are ideal for the formation of snow, and a score of one or 100%, is given. The specific limits for temperature, reflectivity, and velocity, as well as the linear distribution between the cutoff point and 100% point, are shown in Fig. 3.7. Brief explanations of the specific limits and the rules for combining each criterion follow.

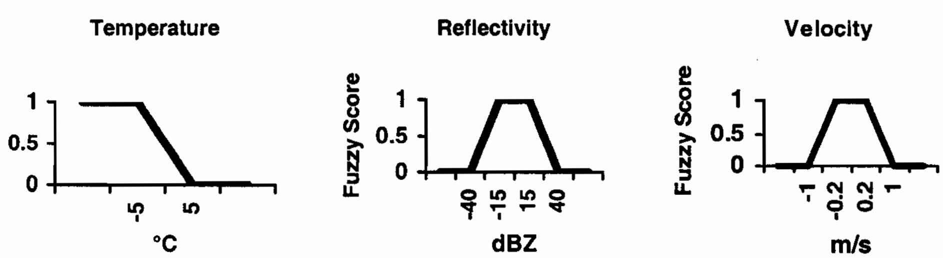

Figure 3.7: Rules for snow detection by fuzzy logic snowscore algorithm. Since velocity changes very little for snow, regardless of its reflectivity, velocity has a peak within 0.2m/s of the idealized relationship. Reflectivity also has a large range of -15 to 15 dBZ.

Temperature cutoff points were based on the regions where enough ice nuclei typically exist for snow to form. Since past observations show that snow can be seen over a wide range of reflectivities, the reflectivity factor score can fall anywhere in the VPR reflectivity range of -40 to 40 dBZ but it usually falls in the middle of this range. Velocity rules are based on a relationship with the ideal ZV relationship for snow. To determine the velocity score, a difference between the velocity at any given reflectivity for the ideal ZV relationship and the observed velocity is calculated. Because snow has a small range of velocities a deviation of more than +/- 0.2m/s from the ideal ZV relationship (3.3) is given a score of 1. If a particles velocity deviates more than +/- 1.0m/s from the ideal relationship they receive a score of zero.

Due to the broad range of acceptable reflectivity values and the unreliability of temperature data, velocity is the most important factor when calculating the total value for the snowscore algorithm. Instead of combining the factors evenly, velocity is given a 60% weight compared to only 20% each for reflectivity and temperature. In the case where no temperature data is available, 80% velocity, 20% reflectivity weights give almost comparable values. The total score given to snow is plotted over the data from 12/10/99 in Fig. 3.8.

3.3.2.2 Verification

Verification of automated algorithms is a very important process. Unfortunately, in the case of the bright band there is little data available to validate the algorithm except the data used to calculate it. Usually verifications are made with aircraft data or an experienced meteorologist's eye. Unfortunately in this case both methods are time consuming, expensive and impractical. A slightly more objective way of validating the algorithm is to plot the score given by this algorithm and compare it to the regions of velocity reflectivity pairs that are expected for snow. Figure 3.8 shows the value calculated by the snowscore algorithm at every point for this case. Comparing this image to the data plotted for 12/10/99 it is clear that the algorithm adequately represents the region of snow.

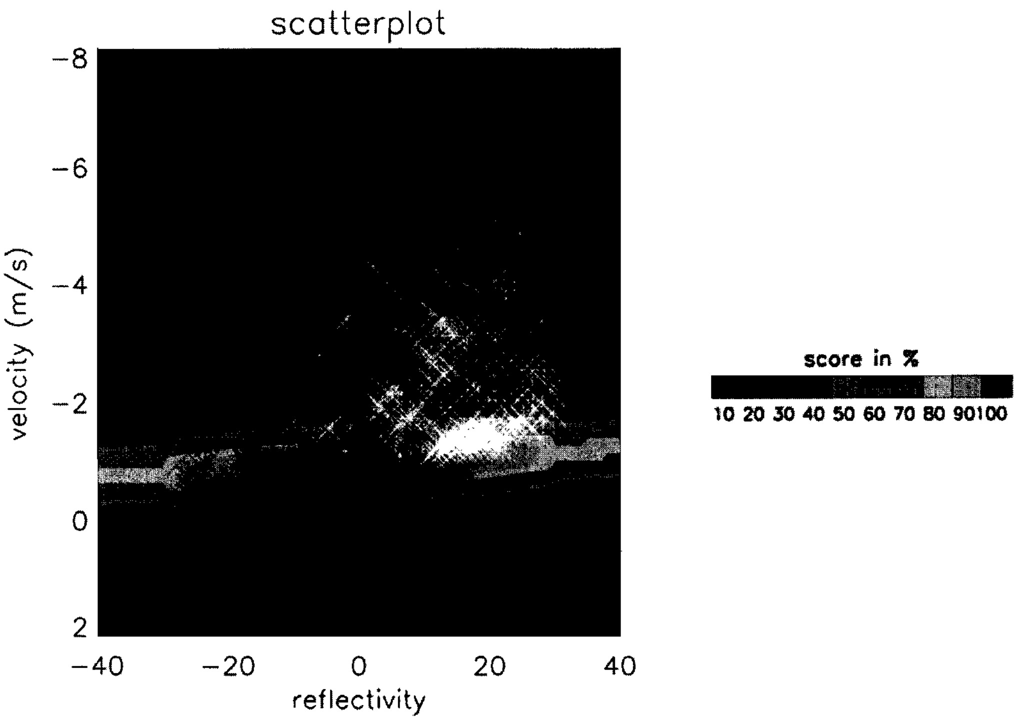

Figure 3.8: General snowscore results plotted over the data from 12/10/99. As before the blue data is from below the bright band (rain), and the white data is the bright band, and the red data is above the bight band (snow). As anticipated, most of the snow in this image falls with in the yellow area corresponding to a snowscore of .9 or higher.

Further verifications of this and other cases will be presented in chapter 5.

3.3.3 Fuzzy Logic Rules for Rainscore Algorithm

As shown for the data gathered at AIRS, the two best ZV relationships for rain are Steiner, (3.6), and the 3rd order fit (3.9). The following section will discuss the advantages and disadvantages of each relationship when using fuzzy logic to determine the likelihood that a hydrometeor is rain. Like for snowscore and the bright band, the process for identifying rain with the VPR and fuzzy logic includes temperature, reflectivity, and velocity factors which are then combined into a final algorithm.

3.3.3.1 Rules

As before, the rules for each factor are fairly simple and are established in much the same way as for the preceding algorithms. The specific limits for temperature, reflectivity, and velocity, as well as the linear distribution between the cutoff point and 100% point, are shown in Fig. 3.9. Brief explanations of the specific limits and the rules for combining each criterion follow.

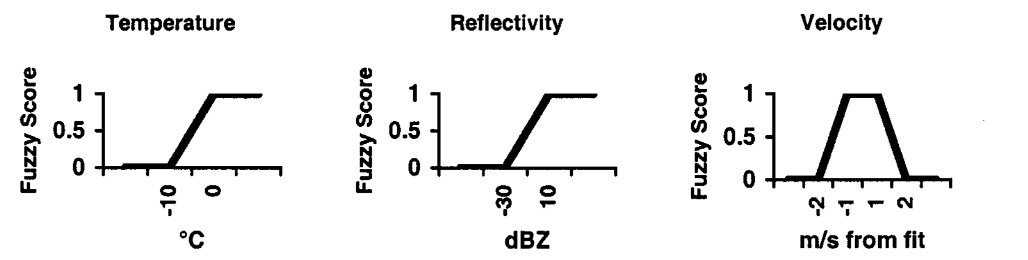

Figure 3.9: Rules for rain detection by the fuzzy logic rainscore algorithm. Velocity has a peak within 1m/s of the idealized relationship, temperature peaks over 0°C, and reflectivity greater than 10dBZ.

Temperature was established in much the same way as it was in the preceding algorithms; however, since the velocity of rain is very dependent on its reflectivity, the criterion for reflectivity and velocity of rain were heavily dependent on the ZV relationship. The greater the reflectivity of rain, the greater the expected velocities for rain, thus rain falling with very small velocities is likely to be drizzle and must be classified as such. To account for drizzle and the fact that the 3rd order relationship is only valid to 0 dBZ, a cutoff is imposed on both relationships for velocities less than -1.5 m/s, which corresponds to a drop size of .4mm or less (drizzle), and greater than -4.5 m/s. Steiner and the third order fit best represent the data for Montreal, but the third order fit was designed specifically with data from Quebec allowing it to give slightly better results.

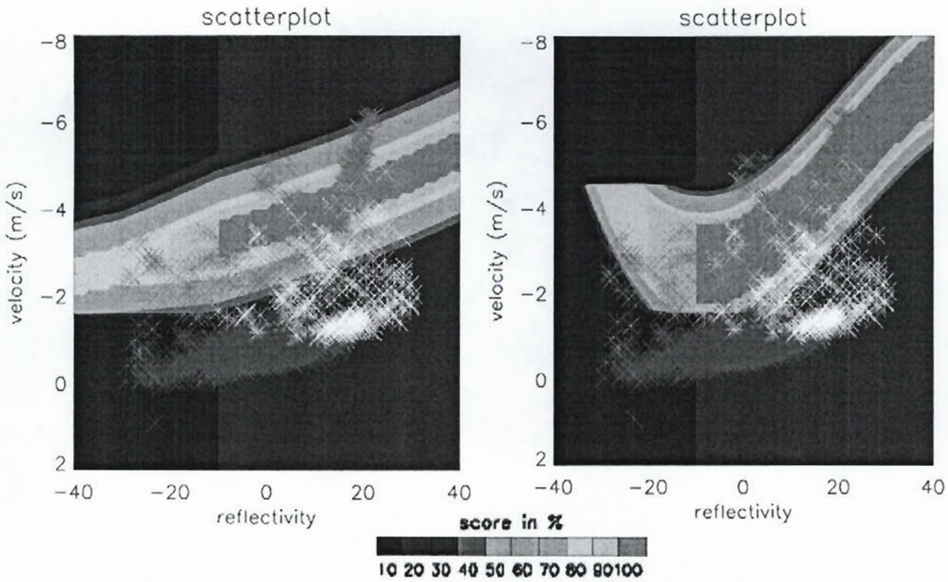

Figure 3.10: General Rainscore results plotted over the data from 12/10/99. The figure on the left used the Steiner relationship and the figure on the right used the third order relationship. In both cases, most of the rain (blue) falls within the red area, corresponding to a rainscore of 1; however, in this case it is clear that the third order relationship fit the data better than Steiner's relationship.

Due to the broad range of acceptable reflectivity and temperature values and the unreliability of temperature data, velocity was considered the most important factor when calculating the total value for the rainscore algorithm. Instead of combining the factors evenly, velocity was given a 60% weight compared to only 30% each for reflectivity and 10% for temperature. In cases where there is no temperature data, 70% velocity, 30% reflectivity weights give almost comparable values. The total score given to rain for each of the two ZV relationship is plotted over the data from 12/10/99 in Fig. 3.10.

3.3.4 Fuzzy Logic Rules for Drizzlescore and Rime Algorithms

Between the characteristics of snow and the characteristics for rain there is an area of drizzle and an area of rime. Both of which are important to identify because they often coincide with SLW. Drizzle is defined by the AMS glossary as "very small, numerous, and uniformly distributed water drops that may appear to float while following air currents to the ground" (Glickman, 2000). Despite the fact that drizzle can be easily confused with light rain or small snowflakes on the radar, it has some unique defining characteristics, such as the fact that it is formed through a warm rain process and thus does not form with a bright band. Another defining characteristic of drizzle is that is does not usually form high above the ground, thus a height limit for drizzle helps to distinguish small snowflakes and drizzle drops.

Rime is defined as "denser and harder than hoarfrost, but lighter, softer, and less transparent than glaze. Rime is composed essentially of discrete ice granules and has densities as low as 0.2-0.3 g cm^{-3}" (Glickman, 2000). The velocity of rime is greater than snow but less than rain. Thus, the idealized ZV relationship for rime is taken as the average of the ZV relationship for rain and the ZV relationship for snow. In addition, rime can be identified by its density, as well as its characteristic increase in fall speed. With the above information, drizzlescore and rimescore algorithms were created.

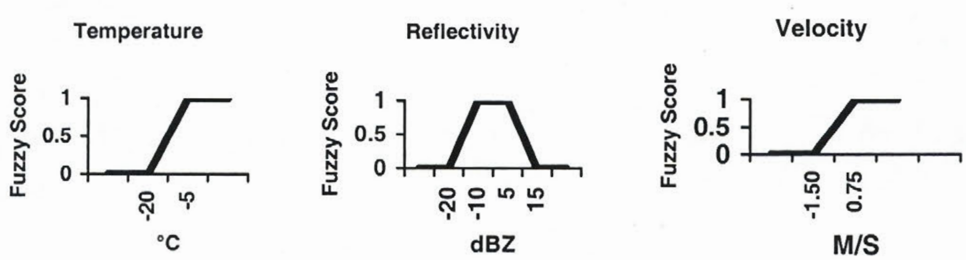

Figure 3.11: Rules for drizzle detection by the fuzzy logic drizzlescore algorithm. Reflectivity has a peak between -10 and 5dBZ, temperature peaks over -5°C, and velocity greater than .75m/s.

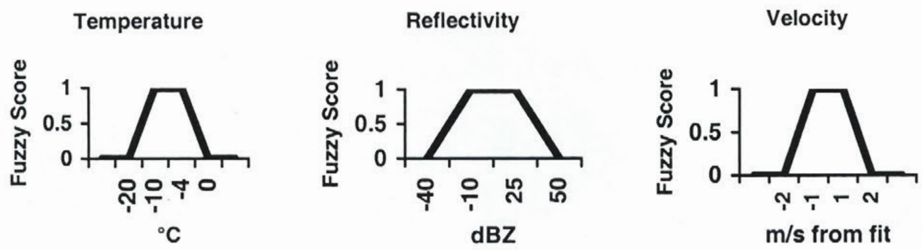

Figure 3.12: Rules for rime detection by the fuzzy logic rimescore algorithm. These two graphs show the fuzzy logic cutoff points for the rimescore algorithm. Reflectivity has a peak between -10 and 25dBZ, temperature peaks between -10 and -4°C. Velocity is taken as the average of the idealized velocity of rain and the idealized velocity of snow.

3.3.5 Final ID

Given all of the information gathered by the rainscore, snowscore, drizzlescore, rimescore and bright band algorithms a final ID can be assigned to all areas of precipitation. The final ID simply identifies each region by the algorithm with the highest score. A verification of the classification algorithms will be presented in chapter 5, but a simple comparison between the raw data (Fig. 2.1) and the final ID (Fig. 3.13) shows good correlation.

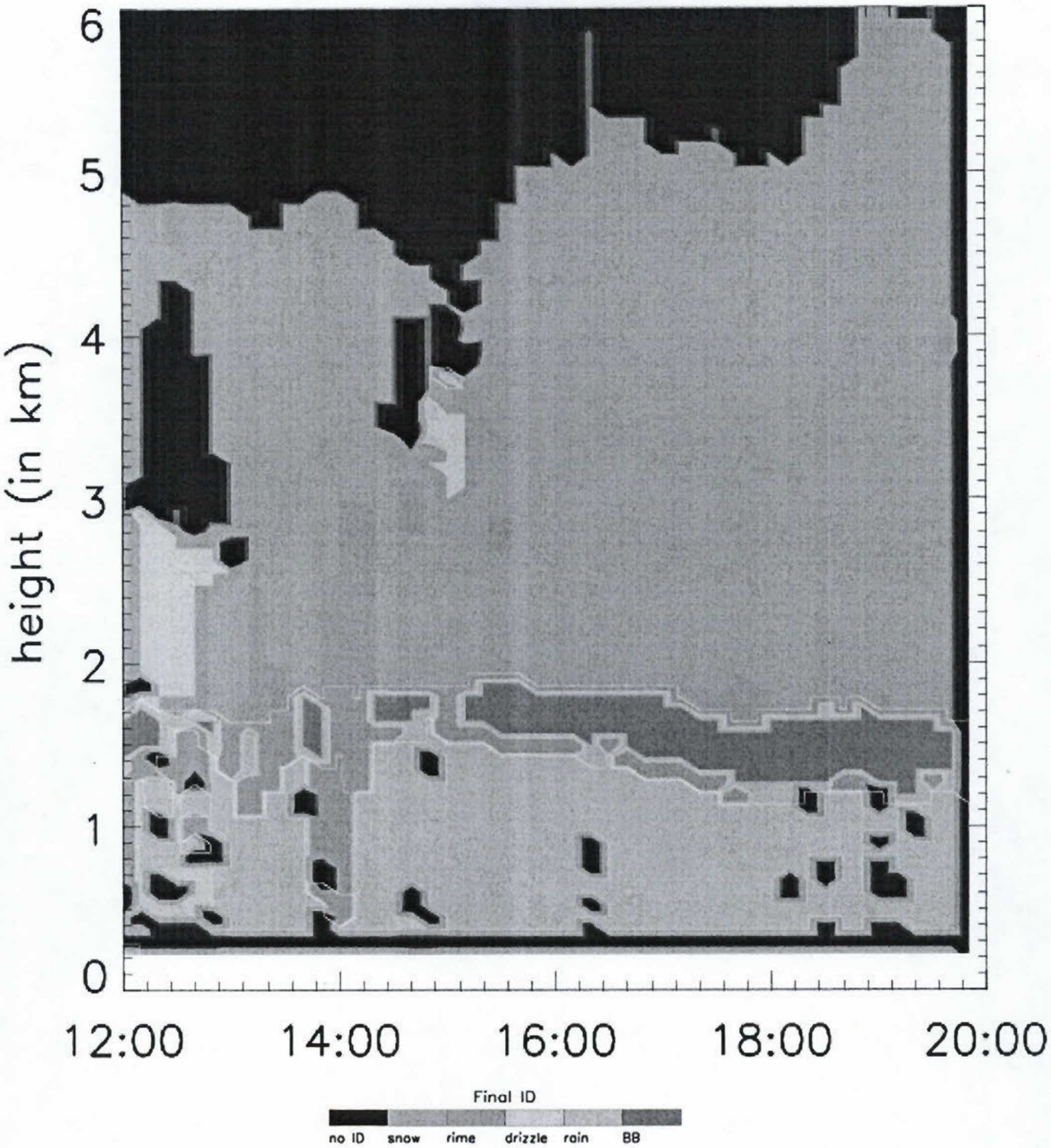

Figure 3.13: Final hydrometeor classification for 12/10/99. Only the main mode of precipitation is shown.

Chapter 4

Mode, Flux and Density Algorithms

In this chapter, the work done hitherto comes together and final calculations are made to find the amount of SLW in the atmosphere. Two algorithms, the snow flux gradient (SFG) and the snow density gradient (SDG), help to accomplish this goal. Since these algorithms are valid only when applied to solid precipitation, the first step is to separate the frozen and liquid precipitation, especially in areas of mixed precipitation. Previous studies of SLW have looked at the value of the SFG and SDG algorithms (Côté, 2002 and Večei, 2002). This study builds upon that work through the separation of modes, preventing the erroneous results that occur when the algorithms are applied to non-frozen or mixed precipitation.

4.1 Mixed Precipitation and Mode Separation Algorithm

Mixed precipitation is defined by the AMS glossary as "Precipitation consisting of a mixture of rain and wet snow which usually occurs when the temperature of the air layer near the ground is slightly above freezing" (Glickman, 2000). In reality, mixed precipitation can include any combination of hydrometeors, and it occurs often in the atmosphere (Cortinas et al., 2004). In this study, identifying mixed precipitation is very important because SLW is often hidden in these regions and thus it is not easily identified. The following sections will explain how spectra data is used, how the mode separation algorithm isolates individual types of precipitation, and finally how mode information will be used in the overall icing algorithm.

4.1.1 Spectra Data

Modes are distinct peaks in the distribution of fall speeds. Modes can be identified from the 128-bin power spectra data at each time and height (hereafter each time and height will represent a different case). For all AIRS dates, spectra data were produced every 30 seconds from the VPR. Before that data could be used, it was corrected for noise and for folding, normalized to the maximum power at each time and height, and plotted on a height versus velocity graph. The first step when working with spectral data was to remove the noise floor. For each case, the noise floor was removed by subtracting the intensity corresponding to the bottom 25th percentile of data (calculated specifically for that case). The next step was to normalize the data for the largest power in each case. After normalizing, the spectral values ranged between zero and one, with one being the value given to the largest power for each case. The vertical profile from each time was then plotted on a velocity versus height plot (Fig. 4.1), which shows the graphical representation of the modes for one 10 min period.

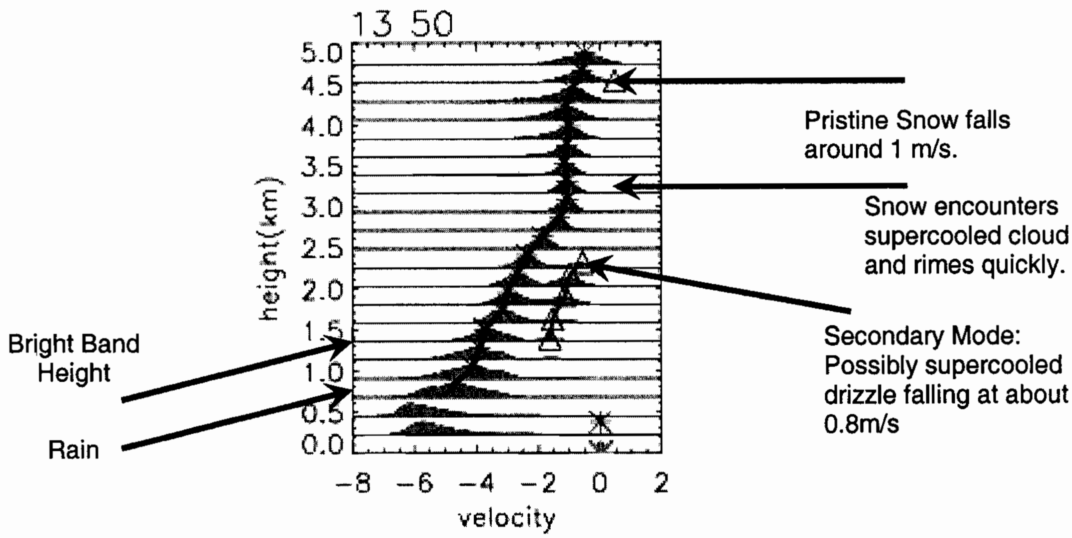

Figure 4.1: This graph shows the modes present during one 10 minute average spectra on 12/10/99. The green shows power normalized by height plotted against fall velocity. Negative velocities by convention travel towards the ground. Note the upper level snow, the rain near the ground, and the two modes co-located between 1 and 2.5 km

Aliasing, the last bias that must be corrected for, occurs as a result of the way that radar data is gathered. Pulses emanate from a source at given time intervals, allowing data that is returned from the targets to be received between pulses. The spectral data contains the power returned at each fall velocity within the Nyquist frequency range of the radar; however, not all fall velocities are initially correct because the unambiguous range of velocity is limited by the Nyquist frequency. Thus the VPR data is mapped on the Nyquist interval, and any values that fall outside the Nyquist frequency will have a velocity that is offset by twice the Nyquist velocity. These values are said to be "aliased". For example, in the above figure a particle with a true velocity of -9m/s would appear to have a velocity of 1m/s. To limit aliasing, the range of velocities must be chosen to include the most likely range of observed velocities. For this reason, the first step taken in this project, when searching for modes, was to find the absolute minimum, which acts as a reference point. The ordered data was then searched from the absolute minimum forward until the 128^{th} point for distinct modes. Ordering the data from the absolute minimum prevents a mode from being split by aliasing and therefore not identified.

4.1.2 Separating the Modes

The objective of this algorithm is to find an average reflectivity and velocity for the main mode, as well as any smaller modes that exist. Finding the modes requires being able to identify all peaks, or local maxima, and where they occur. Several different methods have been attempted to accurately distinguish modes in spectral data, including a mathematically focused method and a pattern recognition method. Initially the mathematical method, an attempt to approximate spectra with functions such as a bi-modal or Gaussian function and then retrieve the parameters of the theoretical curves, was favored. Unfortunately, this method, which was very sensitive to the initial fitting of a function, was plagued by the noisy nature of the data. The more successful method for identifying peaks has been a structured search for local maxima.

In this study, modes were identified through a systematic search for local maxima and minima. Although each local maximum was identified, only the local maxima, M_i, followed by a local minimum, m_i, such that $m_i<0.7\ M_i$ were retained as real local maxima. This was done in order to lessen the sensitivity to noise in the data. Due to the noisy nature of the data, additional limitations were placed on the data, which allowed only 3 possible modes to exist, and required all local maxima to be at least 10% of the absolute maximum.

Once all modes were identified, the average reflectivity and velocity for each mode was calculated over all 128 bins. In cases where only one mode existed, the average reflectivity equaled the sum of the power for each bin, while the average velocity equaled velocity, weighted by power, and averaged. When there were two or more modes, the averages were calculated by summing all the power between the local minima on either side of the peak. This method slightly biased the widest (usually the largest) mode for noise, since the other modes have zero contribution except between the minima on either side of their peak; however, this bias was minimized for by subtracting the noise floor.

By searching the 128-bin spectra data at each height and time for individual peaks in returned power, all modes can be identified. Mixed precipitation can be identified as areas with more than one mode. Looking for vertical patterns in spectra data also helps to segregate mixed precipitation and identify regions of SLW. From this point forward, groups will be referred to as a set of peaks in spectra data that are consistent in height (i.e. the peaks do not vary by more than 0.5 m/s over 75 m). Secondary or tertiary modes are interpreted in the same way as primary modes, and once separated into groups the original mode no longer has any importance.

4.1.3 Interpreting Groups

Interpreting groups provided more information about what type of particles are falling in which areas, and therefore offers a confirm on the results of the snowscore and rainscore algorithms based on physical properties; it also offers a good way to identify the different types of hydrometeors that are present in mixed precipitation. Some bi-model spectra can be a result of drop-drop interactions, but more often the bi-modality is a result of two distinct types of precipitation that are observed together (Fabry and Zawadzki, 2000). For example, some days have rain (formed by the cold rain process) and drizzle (formed entirely as liquid) falling together. In this case the drizzle would be visible as a secondary group, and if it formed above the 0°C isotherm it would be SLW.

Identifying the type of precipitation that composes a group involves looking at the fall velocities and vertical patterns among other pieces of evidence. Fast fall velocities are likely to represent rain, while increasing fall velocities with decreasing altitude are more likely to represent rime. Both snow and drizzle have slow fall velocities, but drizzle rarely occurs high up in the atmosphere. Drizzle does not occur with a bright band in its own group, but drizzle is often found as a second mode near the bright band. If there is a clear bright band, it is unlikely that drizzle will exist in any group significantly above the existing bright band. While no one piece of evidence is decisive, the clues together form a conclusive picture. With respect to aircraft icing, the most interesting and most dangerous secondary groups are found at temperatures below zero, caused by secondary ice generation or supercooled drizzle.

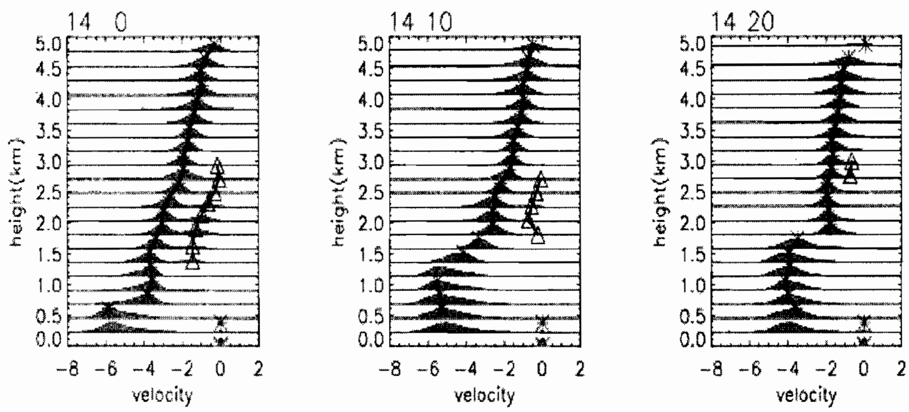

Figure 4.2: This graph shows a time sequence of 10 minute average spectra on 12/10/99. It is interesting to see the large increase in velocity in the main mode (green) due to riming associated with the presence of a secondary mode (blue). By 1420, there are two clear regions with a discontinuity between them, which implies a melting layer. Where there is no secondary mode (1420), there is also no large increase in velocity in snow.

4.1.3.1 Using Modes to Identify SLW

One of the biggest clues used to identify regions of SLW is riming. If snow is present in the same region as SLW, water will freeze onto snowflakes as they fall. Likewise, if an aircraft is in a region with SLW, water will necessarily freeze onto the aircraft if the body or control surfaces are below 0°C. While it is possible to visually infer riming from an increase in velocity on the power spectra plots, the next two algorithms offer a more consistent method to recognize riming. However, these algorithms can only be applied to solid or frozen precipitation, so at this point the results of the mode separation algorithm and classification algorithm can be used as input for the SLW quantification algorithms. In Chapter 5, results from all of the algorithms will be compared with verifications for several different days.

4.2 Snow Flux Gradient (SFG) Algorithm

The snow flux gradient, developed by Zawadzki et al., (2000) and used by Bell (2000), Côté (2002), and Večei (2002) in their McGill masters theses, offers an excellent way to measure LWC and identify regions of SLW. This study differs from past projects in that the algorithm was only applied to areas that received a final classification ID as snow or rimed snow. By separating out the groups and using the classification algorithms to apply the SFG only to the frozen precipitation, which it is designed for, this study reduces errors in calculated LWC.

4.2.1 Mass Flux

Mass flux, defined as the product of the mass and fall speed, is a way to measure the growth of particles or the precipitation rate. To calculate mass flux, one needs mass-weighted velocity and mass, both of which can be calculated with the information given by the VPR. Using a relationship from Zawadzki et al., (1993), mass (M_s given in kg/m^3) can be derived from reflectivity as shown in (4.1):

$$M_s = 10^{-5} Z_s^{0.5} \tag{4.1}$$

and mass-weighted velocity can be calculated from the Doppler velocity, assuming a Marshall-Palmer distribution. The Doppler velocity is multiplied by a factor of .8505 to go from reflectivity weighted to mean mass-weighted velocity (W. Szyrmer, 2004, private communication).

Calculating flux is advantageous because small changes in reflectivity and velocity are magnified when they are multiplied together, making any change more obvious. It is important to know which processes lead to the increased mass flux when using flux to identify regions of SLW. Flux growth, when calculated with mass derived from reflectivity, can be real, as a result of riming or deposition, or can be fictional if it is a result of aggregation.

The three main sources of increased radar-estimated mass flux are: aggregation, vapor deposition, and accretion of cloud. Aggregation leads to large reflectivities due to particle growth. This can cause unusually large mass flux changes because mass is calculated from reflectivity (4.1). In other words, when viewed from the radar, the aggregated snowflakes have a high reflectivity and thus result in a perceived growth in mass, despite the fact that there is no real change in mass. Vapor deposition leads to true mass growth of the cloud or precipitation particles; however, when co-located with SLW this effect is small enough to basically ignore (Koenig, 1972). Finally, accretion of liquid cloud is another process leading to increased snowflake size due to the SLW that freezes and rimes onto crystals. Understanding the reason for these changes in flux facilitates identifying regions of SLW.

4.2.2 Mass Flux Gradient

Using the gradient of mass flux, a calculation can be made to quantify LWC. Assuming a steady state, where there is no change in saturation (s), LWC is calculated based on the following relationship:

$$\frac{ds}{dt} = wG - DEP - CND = 0 \quad . \tag{4.2}$$

In other words, generation of supersaturation by vertical air motion (*wG*) is equal to the sum of deposition onto snow and the condensation of water. Assuming that cloud particles are small compared to snowflakes, it is a logical assumption that the collection efficiency of snow is high and that if cloud liquid water content is maintained, surplus water can be deposited or rimed onto the snow. Thus (4.2) can be expressed as:

$$wG = DEP + RIM \tag{4.3}$$

where RIM is the amount of riming. This relationship holds true as long as the rate of vertical motion stays relatively steady or changes more slowly than the other variables.

The next steps in calculating the LWC are presented in more detail in Zawadzki et al., (2000). Generally speaking, these steps require a calculation of the rate of snow crystal growth by riming, the thermodynamic constrains, and conservation equation for precipitation described by Kessler (1969). Calculating the riming rate assumes an exponential size distribution for the snow particles ($N(D_s) = N_{os}e^{-\lambda D_s}$), a geometric sweep-out, and a constant collection efficiency. These three considerations yield the relationship:

$$RIM = \beta M_c M_s^{0.82} \tag{4.4}$$

where RIM is in kg m^{-3} s^{-1} , M_c is the content of condensed water in kg m^{-3}, M_s is the content of snow in kg m^{-3}, and β is the thermodynamic constant given by:

$$\beta = .093EN_{os}^{0.18}\left(\frac{\rho_o}{\rho_a}\right)^{0.5} \quad . \tag{4.5}$$

In this relationship β is dependent on temperature through N_{os} (given in m^{-4}) and E is the collection efficiency set to 0.5. The density correction factor ($\left(\frac{\rho_o}{\rho_a}\right)^{0.5}$), based on a standard atmosphere, is used when calculating the equivalent rain velocity and reflectivity values to correct for the decreasing air density with altitude. The value of 0.093 has been obtained assuming bulk snow density of 100kg m^{-3}, and snowflake fall-speed-diameter relationship (4.6) with $a=5.1m^{1-b}s^{-1}$ and b=0.27.

$$v_s = a_s D_s^{b_s}. \qquad (4.6)$$

N_{os} is defined as:

$$N_{os} = 2*10^6 e^{\frac{T_o - T}{8.18}}, \qquad (4.7)$$

where the temperature (T) is measured in Kelvin and T_o is 273.15 K.

To continue, the rate of snow growth by deposition has been obtained with an assumption of thermal equilibrium on the surface of the snowflake. This leads to:

$$DEP = DEP\big|_{Mc=0} - \chi RIM, \qquad (4.8)$$

a description of the bulk change in deposition given riming, where $DEP\big|_{Mc=0}$ is deposition in the absence of liquid water. In this equation χ is a thermodynamic constant. When substituted into (4.3), this becomes:

$$wG = DEP\big|_{Mc=0} + (1-\chi)RIM. \qquad (4.9)$$

Finally (4.4) and (4.9) can be plugged into Kessler's (1969) equation for snow conservation giving:

$$M_c = \frac{1}{\beta(1-\chi)M_s^{0.82}}\left[\frac{\dfrac{\partial M_s\overline{V}_s}{\partial z}}{1-\dfrac{1}{G}\left(\dfrac{\partial M_s}{\partial z}+\kappa M_s\right)} - DEP\Big|_{M_c=0}\right] \tag{4.10}$$

where V_s is the mean mass-weighted snow fall speed and κ is the air compressibility term. To further simplify this equation, the thermodynamic constant, χ, is assumed to be much smaller than one and deposition is negligible compared with the first term in the brackets, for usual atmospheric conditions. In general it is safe to assume that riming is a larger contributor than deposition in conditions where SLW is likely to exist (Zeng *et al.*, 2000, Koenig, 1972). Thus, the following relationship is used:

$$LWC = M_c = \frac{1}{\beta M_s^{0.82}}\frac{\partial M_s\overline{V}_s}{\partial h}. \tag{4.11}$$

4.2.3 Results Using the SFG

The SFG was applied to regions where the snowscore results were greater than 0.4. Negative values from the SFG algorithm correspond to areas of evaporation or regions that are not saturated with respect to water while positive values correspond to riming. Maximum riming regions correspond to the areas where the mass flux gradient is changing the most (Côté, 2002). The following figure shows the mass flux results and the mass flux gradient results from 12/10/99. More examples will be shown in Chapter 5.

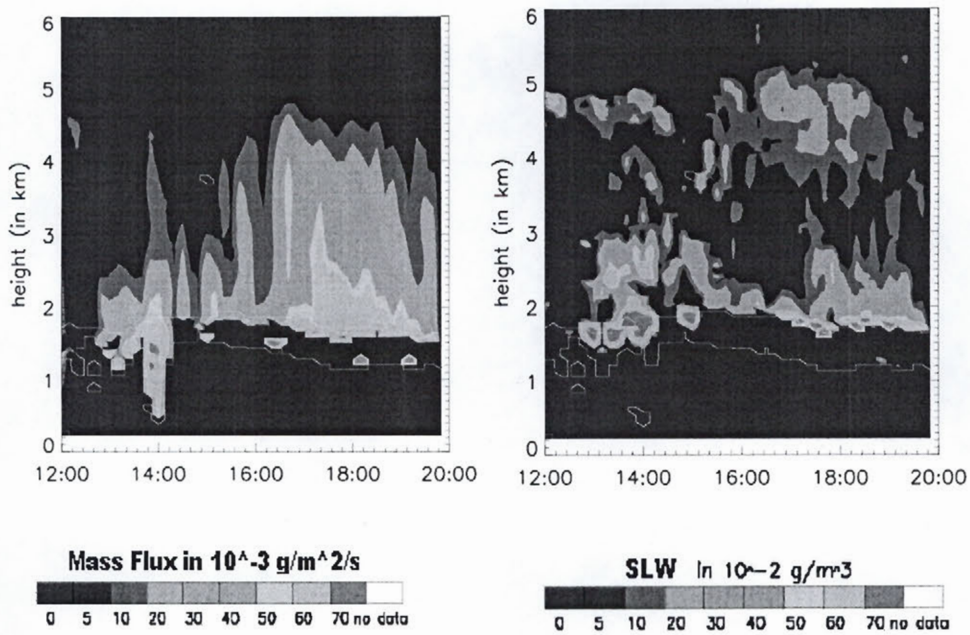

Figure 4.3: On the left is the mass flux of snow and on the right is the result of the SFG algorithm.

4.3 Snow Density Gradient (SDG) Algorithm

The snow density gradient is another way to find areas of SLW based on the Doppler velocity and reflectivity given by the VPR. Like the SFG algorithm, it has been applied in previous instances (Večei, 2002). Also like the SFG, the SDG only provides valid results when applied to frozen precipitation, which was not previously possible. In addition, the SDG has an advantage that it is not affected by aggregation because it has a velocity focus rather than a reflectivity focus.

4.3.1 Calculating the Snow Density Gradient (SDG)

It is known that riming causes snowflakes to increase in density (Mitchell *et al.*, 1990), thus if one can calculate the change in density, then one can know the quantity of SLW. The SDG algorithm compares the Doppler velocity and reflectivity for snow to the expected Doppler velocity and reflectivity of equivalent rain to calculate the density of snow. Based on the assumptions that the mass changes only due to riming and that the snowflakes do not change size as a result of riming, the following equation is used to calculate LWC (Rogers and Yau, 1996):

$$\frac{dm_s}{dh} = \frac{\pi D_s^3}{6}\frac{d\rho_s}{dh} = \frac{\pi}{4}D_s^2 EM_c \tag{4.12}$$

where M_c is the LWC, m_s is the mass of snow, ρ_s for the density of a snow, D_s as the radius of the snowflakes, h as the height, and E as the accretion efficiency. The basic steps needed to find the LWC include: calculating the equivalent flux of rain by calculating the equivalent reflectivity and Doppler velocity of rain, finding the average (bulk) density of snow using the ratio of the snow and rain velocities, and calculating the average (bulk) radius of snow. This information leads to a final calculation of LWC based on the changes in density.

Step one is to calculate the equivalent flux for rain. This step requires a ZV relationship to calculate the equivalent velocity for rain. In this case Steiner's (1991) equation is used for consistence with past work:

$$\overline{V_r} = 2.95 Z_r^{0.098}\left(\frac{\rho_o}{\rho_a}\right)^{0.5}. \tag{4.13}$$

In this equation, $\overline{V}$ is used to represent velocity weighted by reflectivity, likewise all subsequent equations in this algorithm will represent any variable weighted by reflectivity in the same way, for example x weighted by reflectivity would be $\overline{x}$.

The density correction factor ($\left(\frac{\rho_o}{\rho_a}\right)^{0.5}$),based on a standard atmosphere, is used when calculating the equivalent rain velocity and reflectivity values to correct for the decreasing air density with altitude. The air density any given height can be calculated with the ideal gas law:

$$\rho_a(h) = \frac{P(h)}{RT(h)}. \tag{4.14}$$

From here forward ρ_0 is taken as the reference density at the surface and is $1.2 kgm^{-3}$. To actually solve for the Doppler velocity of rain equivalent precipitation, the following equation is solved:

$$\overline{V}_s Z_{se} = \overline{V}_r Z_r = \overline{V}_r \left(\frac{\overline{V}_r}{2.95\left(\frac{\rho_o}{\rho_a}\right)^{0.5}} \right)^{1/0.098} . \tag{4.15}$$

where Z_{se} is the reflectivity of snow correcting for the ratio of the dielectric constants ($\left\| \frac{K_r^{\,2}}{K_s^{\,2}} \right\|$).

Step two in the SDG algorithm uses the calculated reflectivity and Doppler velocity for the rain equivalent to calculate the average or bulk density of the snow. From (4.15):

$$v_s(D_s)dZ_{se}(D_s) = v_r(D_r)dZ_r(D_r), \tag{4.16}$$

where v_s and v_r are velocities of individual particles. The assumptions that the ratio of an individual snowflake velocity and individual raindrop velocity is equivalent to the inverse ratio of their radii, and that the particles take a spherical form lead to:

$$\frac{v_r}{v_s} = \frac{D_s}{D_r} = \left(\frac{\rho_r}{\rho_s}\right)^{1/3} \tag{4.17}$$

When (4.17) is introduced to (4.16) and integrated over dZ for the whole distribution

$$\overline{\rho}_s = \rho_r \left(\frac{\overline{V}_s}{\overline{\overline{V}}_r} \right)^3 . \tag{4.18}$$

where ρ_r is 1000 kg m^{-3}.

The final step in the SDG algorithm involves relating the snowflake density change to the amount of liquid water. From (4.12) one can write

$$\frac{d\rho_s}{dh} = \frac{3}{2D_s} EM_c. \tag{4.19}$$

Then taking the integral of (4.19):

$$\int \frac{d\rho_s}{dh} dZ_{se} = \frac{3}{2} EMc \int D_s^{-1} dZ_{se} \tag{4.20}$$

and using (4.16) and (4.17) this relationship can be expressed as:

$$M_c = \frac{d\overline{\rho}_s}{dh} \frac{2}{3E} \overline{D}_r \frac{Z_{se}}{Zr}. \tag{4.21}$$

if $\left[\overline{D_r^{-1}}\right]^{-1} \approx \overline{D}_r$ and is the reflectivity weighted raindrop diameter obtained from a Marshall-Palmer drop size distribution (M-P DSD)

$$\overline{D}_r = \frac{7}{\Lambda} = 7\left(\frac{Z_r}{N_o 6!}\right)^{1/7}, \tag{4.22}$$

where Λ is the slope parameter of the M-P DSD and N_o is the intercept at 0.08cm^{-4}.

Thus a final value of LWC is obtained from (4.21) with the aid of (4.15):

$$M_c = \frac{\Delta\overline{\rho}_s}{\Delta h} \frac{2}{3E} \overline{D}_r \frac{\overline{V}_r}{\overline{V}_S} \tag{4.23}$$

Where $\overline{\rho}_s$ is from (4.18), Δh is 75m, E is 0.5 .

4.3.2 Results Using the SDG

After solving (4.20) it is clear that LWC is directly proportional to the gradient of snow density. Furthermore, since the calculations are all based on a co-location with snow it is safe to assume that all the LWC is actually SLW. The following figure shows the SDG gradient for 12/13/99. More detailed examples with verifications will follow in chapter 5.

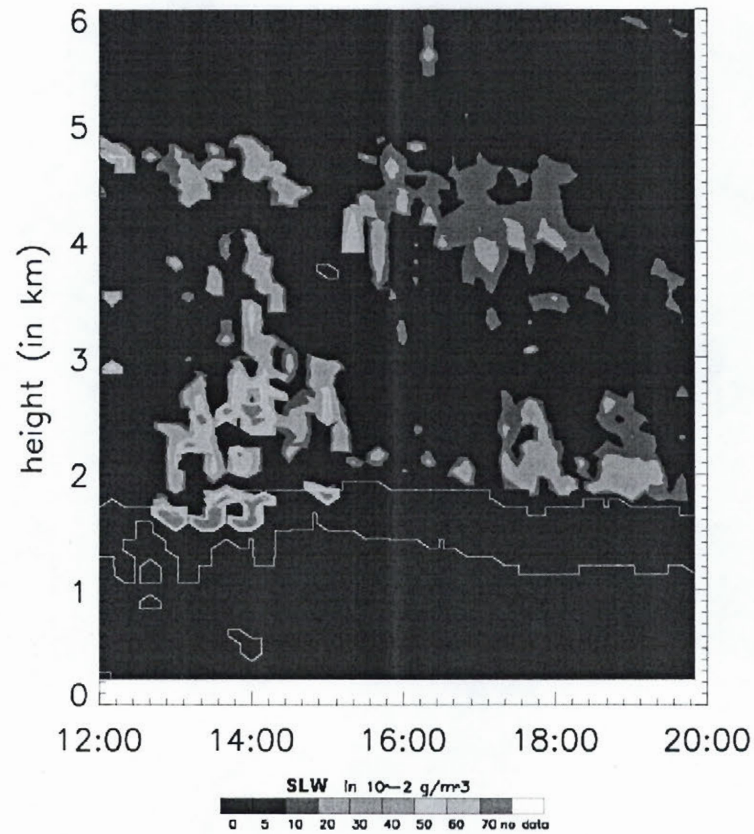

Figure 4.4: This graph shows the results of the SDG algorithm.

Chapter 5

Results and Verifications

Case studies are useful to validate the claims made by the above algorithms. The preceding sections have had examples from December 10, 1999, thus a brief discussion of that day followed by some verifications will be presented first. The rest of this chapter will cover 2 additional case studies from the AIRS field project: December 13, 1999, and December 16, 1999. Each case includes features that often provide challenges for icing systems, and was chosen for the availability of verification data.

5.1 December 10, 1999, the bright band

5.1.1 Raw data/spectra

December 10th was an interesting day that, for the most part, offered clear snow, clear rain, and a well defined bright band, but also had some mixed precipitation and some SLW. Looking back to chapter 2, the raw data can be seen in Fig. 2.1. This image shows clear rain, snow, and bright band signals, with only a hint of information available about SLW or any areas of mixed precipitation. Spectra available in Fig. 4.1 and Fig. 4.2 provide more detailed information about these regions of possible SLW.

5.1.2 Classification of Final ID

Once the data has been separated into groups the next step was to apply a series of classification algorithms. The bright band algorithm was applied first to the data in general, and then the snowscore, rimescore, drizzlescore and rainscore algorithms were applied to the data by groups. The result of the bright band algorithm can be seen in Fig. 3.3 and compares nicely with the horizontal line visible in the raw data (Fig. 2.1). The bright band algorithm was calculated first so its results could be used in the other classification algorithms.

The results of the rainscore, snowscore, drizzlescore and rimescore algorithms are shown below in Fig. 5.1. Note, where there was more than one mode visible in the spectra (white regions) there is no score given. In regions with overlapping groups individual ID score were given for each group (not shown).

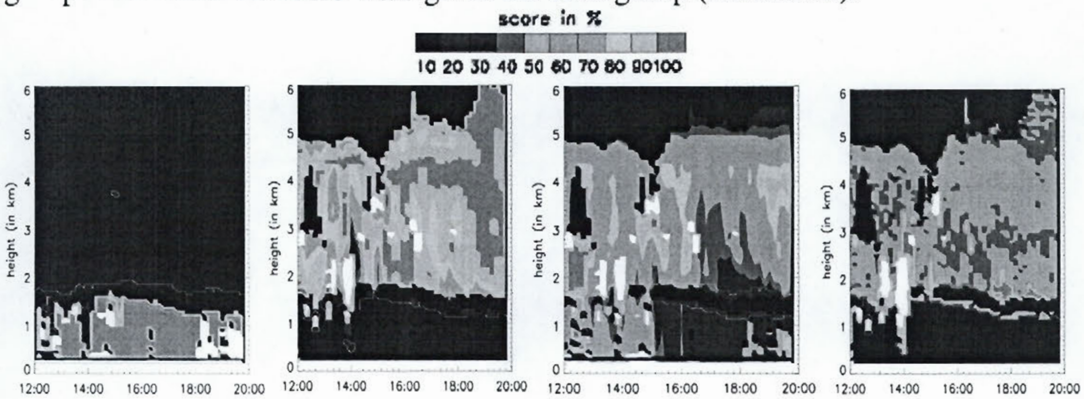

Rainscore Snowscore Drizzlescore Rimescore

Figure 5.1: From left to right are the fuzzy logic results of the rainscore, snowscore, drizzlescore and rimescore algorithms. The white areas are areas that had more than one mode and thus separate classifications must be done for each mode.

Next a final ID, Fig. 3.13, is given to the precipitation in each region. The final ID corresponds simply to the classification algorithms that have the highest score.

5.1.3 Verification of Classification

To verify the classification algorithms both surface and upper air data were used. Since the VPR data is in UTC, all verifications are also presented in UTC, although the surface observations were given in local (Eastern Standard) time, and thus were adjusted to match the radar observations. Relative humidity, temperature, and reports of weather were the most useful data to verify the algorithms.

For December 10, 1999 there was rain reported at every hour between 1300 UTC and 2000 UTC, according to the surface reports from AIRS at Mirabel (YMX GRP118 1999). The image below (Fig. 5.2) shows a plot of the AIRS surface observations for relative humidity and temperature.

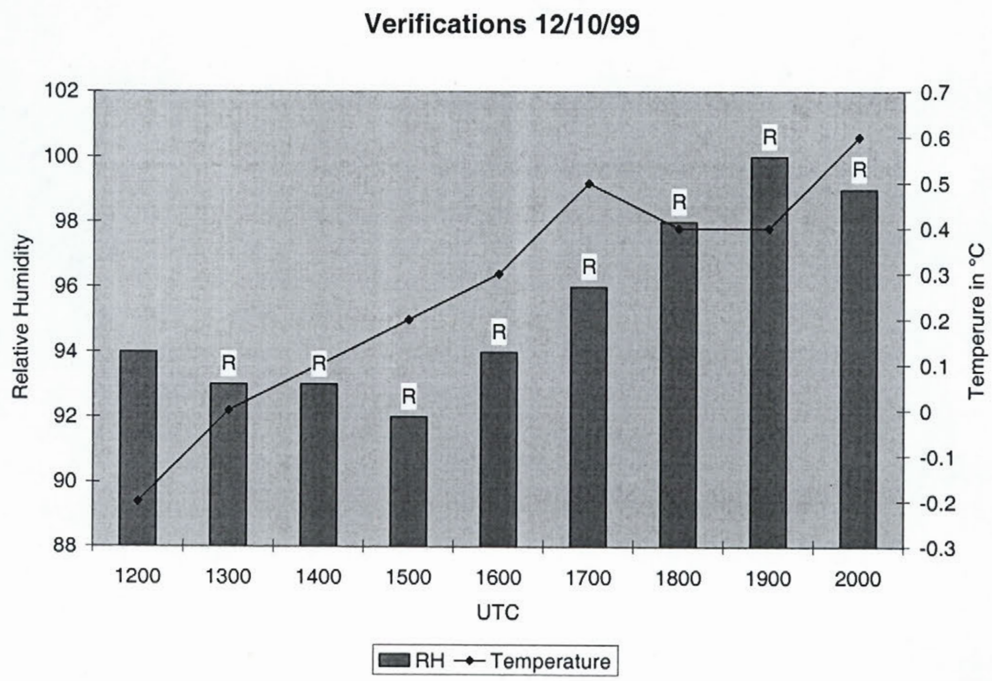

Figure 5.2: Surface observations of relative humidity and temperature from Mirabel on 12/10/99. The R is reported above the RH bar when rain is recorded in the observation.

For more detailed information, the TP/WVP3000 radiometer recorded rain occurrences at 9 minute intervals over the whole period (Fig. 5.3). The better time resolution enhances the surface observations.

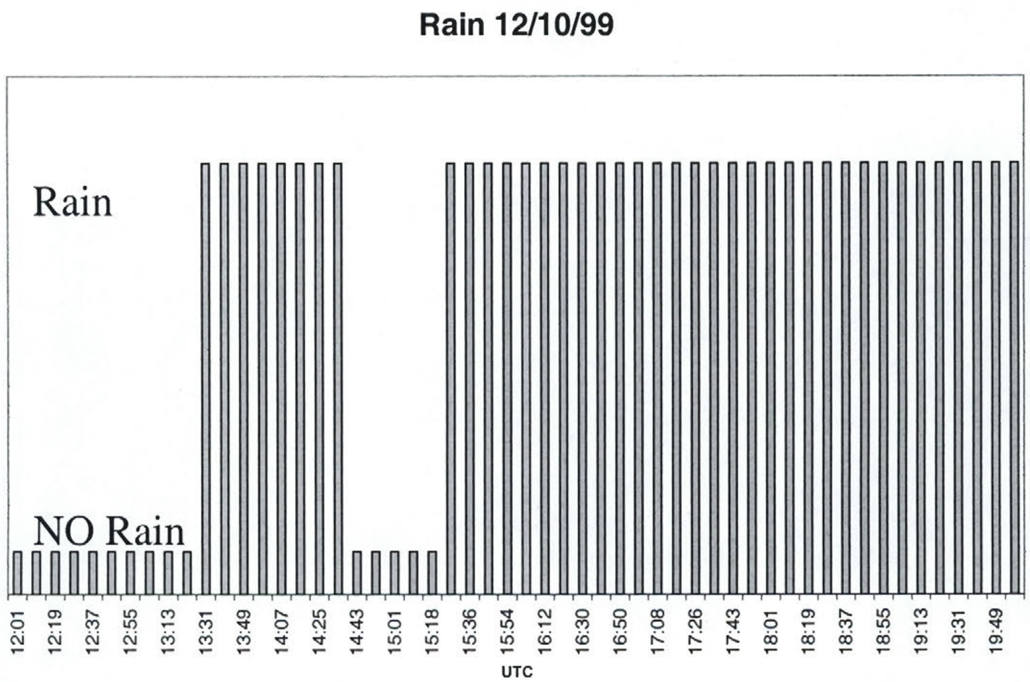

Figure 5.3: Rain occurrences from the TP/WVP3000

The relative humidity is high for the entire period, but increases steadily after 1500. This corresponds nicely with the time when the algorithms show the bright band as well defined, with rain falling below. At 1300 the algorithm and the surface observations are both reporting rain but the radiometer does not pick it up until 1331. This is possibly because the rain is so light it is below the radiometers detection threshold, or possibly because the temperatures are still so close to zero some of the particles are still frozen and the radiometer is not detecting them. At the surface all three sources are reporting rain. Temperature, which was below zero and is just reaching 0°C at 1400, confirms the possibility of riming, especially slightly above surface level.

To validate upper level classifications, soundings and pilot reports are used. For December 10th soundings from Mirabel were available at 1415 UTC (Fig. 5.4) and 1715 UTC (Fig. 5.5):

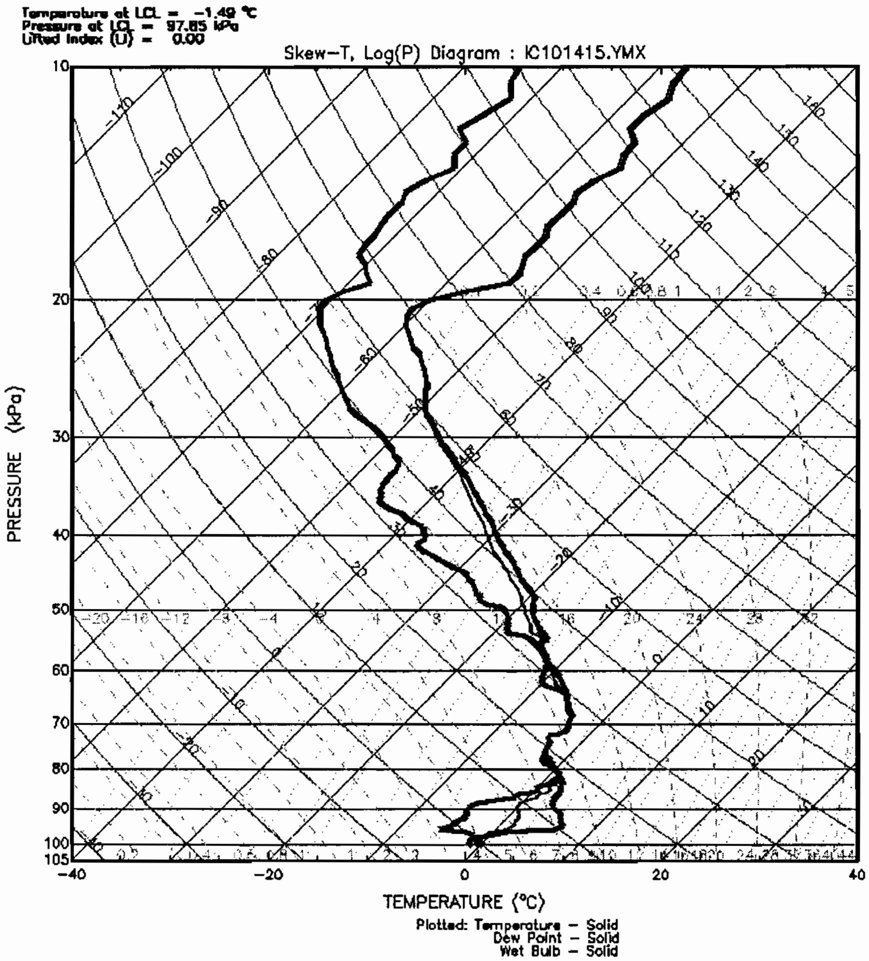

Figure 5.4: Sounding from Mirabel at 1415 UTC on 12/10/99

The sounding from 1415 UTC offers a good insight into the vertical column above the airport. According to this sounding the column is saturated at the surface and then again above 2 km. There is a moist adiabatically unstable layer around 2 km (800 hPa) suggesting the potential for an updraft and liquid water. In the middle of this layer the profile transitions across the 0°C isotherm. These features on the profile imply that with any forcing there will be strong updrafts and conditions ideal for the formation of liquid water. Since the temperature is so close to zero the possibility is ripe for the formation of SLW. After a small stable area the profile is essentially moist adiabatic above 3 km (700 hPa).

The groups (snow and drizzle) visible in Fig. 4.2 are supported by this structure. The unstable layer seen in figure 5.4, combined with an updraft, creates conditions favorable for the formation of liquid water. Snow formed aloft falls into the unstable layer, absorbing some of the SLW and becoming rimed, as diagnosed in the final ID (Fig. 3.13). While the updraft is maintained the formation of SLW is greater than the rate at which the snow is being rimed and thus the second mode of supercooled drizzle is formed. Above 5 km there is no longer any precipitation in the sounding or in the algorithm results, and by the time the precipitation reaches the ground it has mostly melted into rain.

A second profile taken at 1715 UTC shows a simpler profile for the second half of December 10, 1999: In this sounding there is a saturated, stable, surface inversion layer, followed by almost 3 km of slightly less stable saturated air, eventually drying out. The sounding transitions across the 0°C isotherm just below 2 km (800 hPa) which confirms the algorithms' results that suggest a bright band and snow-rain transition. This sounding has no unstable regions suggesting updrafts or SLW formation, confirming the algorithms detection of simply snow melting into rain.

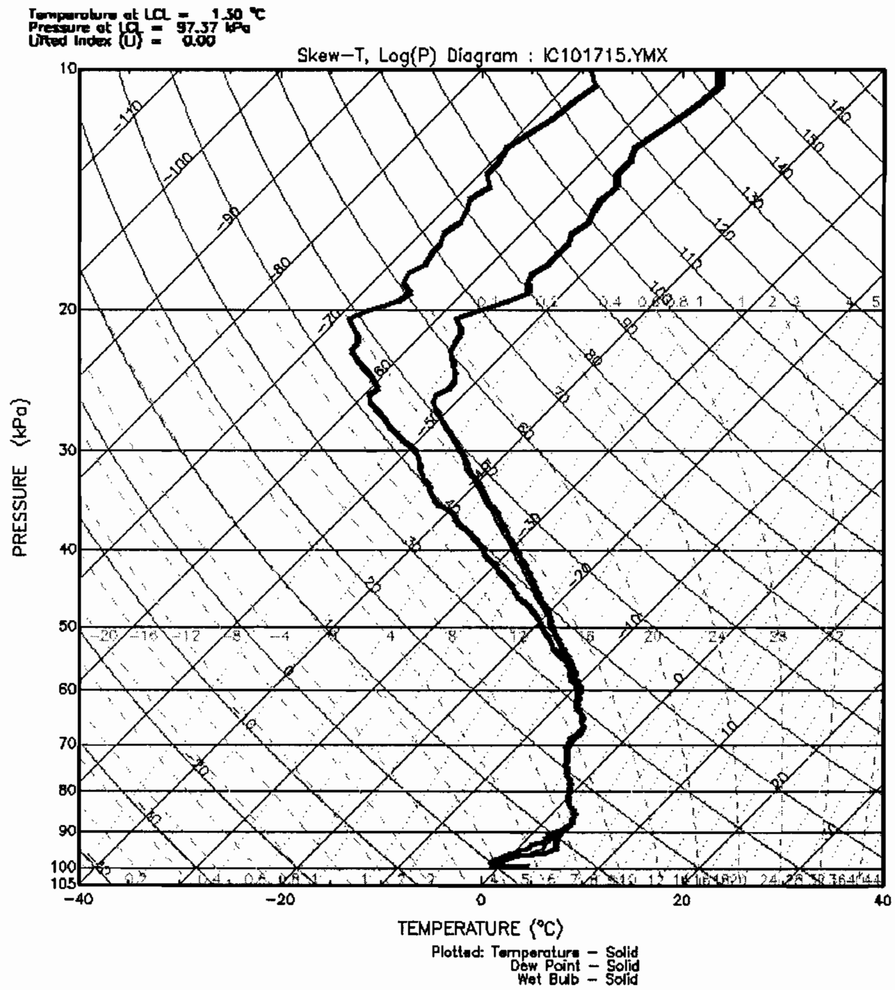

Figure 5.5: Sounding from Mirabel at 1715 UTC on 12/10/99

Aircraft also offer good verification for upper levels, but they only provide data for limited locations and times. On December 10th there was an aircraft in the region just before 1500 experiencing icing, and one after which found nothing, both of which help to confirm the classification for that time period.

5.1.4 SFG and SDG

Based on the areas identified as frozen precipitation in the final ID, the SFG and SDG algorithms were applied. The results of these algorithms are shown in Fig. 4.3 and Fig. 4.4 respectively. The two algorithms agree nicely; however, there are some differences. The biggest difference to note is the region just above the bright band where the SFG algorithm has higher values than the SDG algorithm. This is possibly a result of aggregation effects or possibly a result of the algorithm mistakenly detecting part of the bright band.

5.1.5 Verifications

To validate these results Fig. 5.6 shows a plot of integrated liquid water content (ILWC) from the SDG (pink), the SFG (red), and two radiometers, (light blue) for the WVP-1100, (dark blue) for the TP/WVP3000.

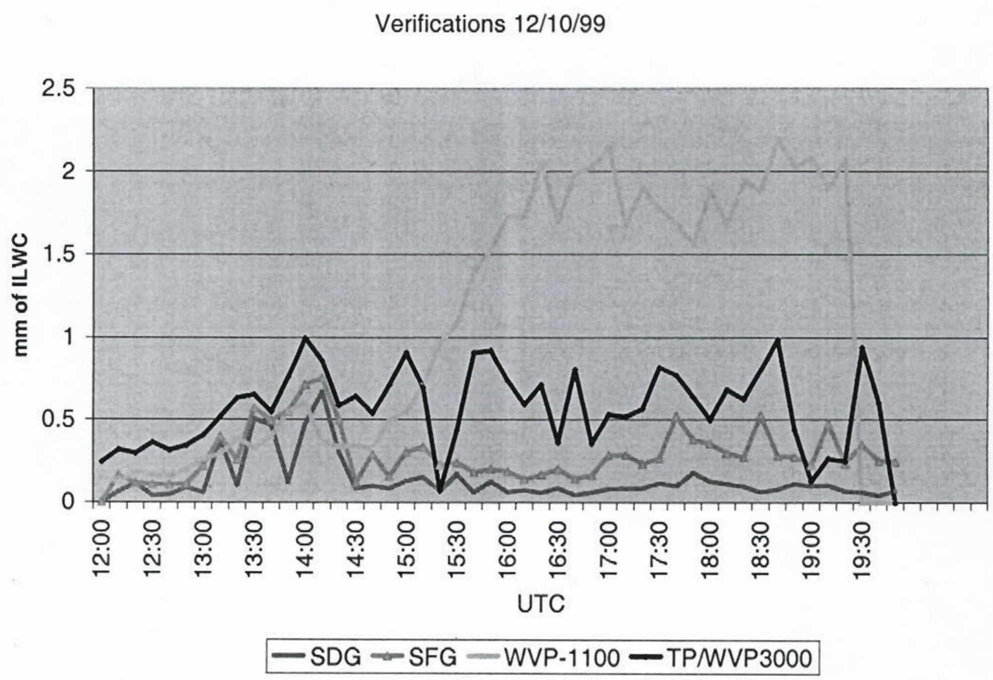

Figure 5.6: Verification of SFG and SDG algorithms against two radiometers using Integrated LWC.

The most notable feature in this plot is the explosion of ILWC values from the two radiometers after 1500. This explosion occurs at the same time as the surface observation and algorithms report heavier liquid precipitation. Under circumstances like that, radiometer data becomes unreliable. Radiometers are notorious for giving unrealistically high readings in rain, and thus the high ILWC values from the WVP-1100 after 1500 must be ignored. The TP/WVP3000 is slightly better since it is equipped with a fan designed to keep its sensor dry; however, even after 5 years of design improvement, the TP/WVP3000 was still having problems keeping its sensor dry during the heavier precipitation experienced at AIRS II.

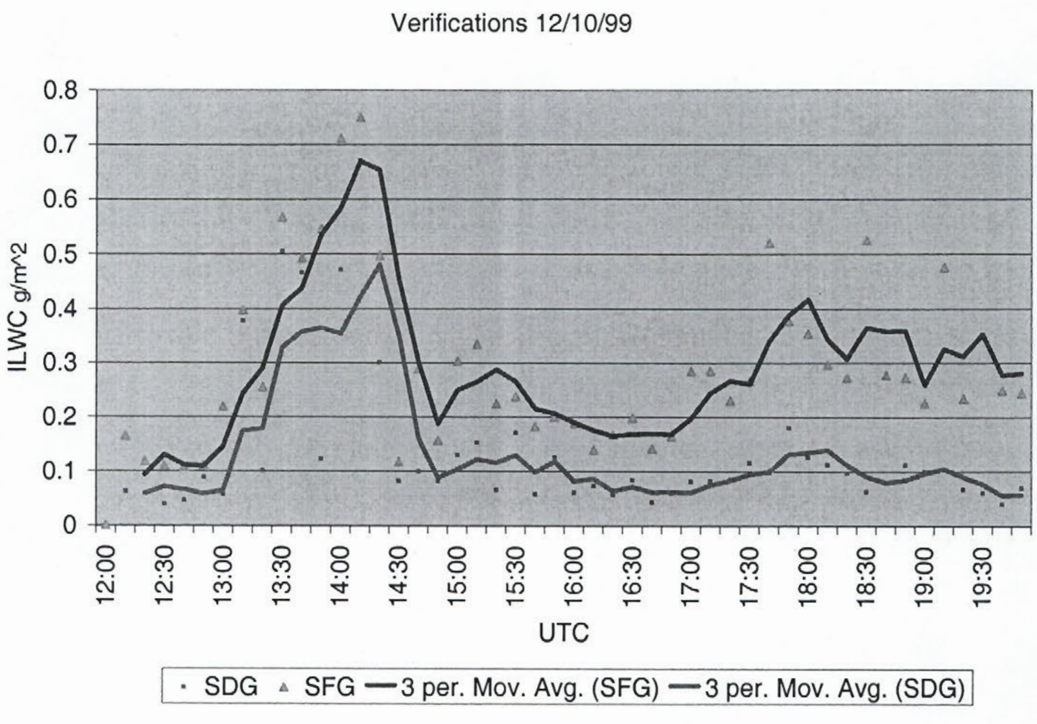

Figure 5.7: Thirty minute average of SFG and SDG for 12/10/99

The SFG and SDG algorithm are consistent, although the SFG is consistently greater. The two algorithms peak in about the same place and at the same time as the sounding suggests liquid water, and the spectra (Fig.4.2) are showing bimodality. There was also a report by one of the AIRS research aircraft (the

Twin Otter), that encountered severe icing between 1454 and 1501 UTC, just below 3900m (around 12,700 feet). The aircraft reported liquid water contents between 0.1 and 0.3 g m^{-3} (Isaac *et al.*, 2001), which is the same range the SFG and SDG were reporting LWC.

5.2 December 13th 1999, drizzle and snow

5.2.1 Raw data/spectra

December 13th was an even more interesting day to study mixed precipitation, drizzle and SLW. The raw data, shown below in Fig. 5.8, is deceptively simple. The ZV data does not show any kind of bright band, nor is there any rain in the image; however, there is some hint of drizzle aloft around 1400. Spectra data is also available for the whole period, but is most interesting for the period between 1300 and 1500 (Fig. 5.9) where two groups are co-located and more detailed information is desired.

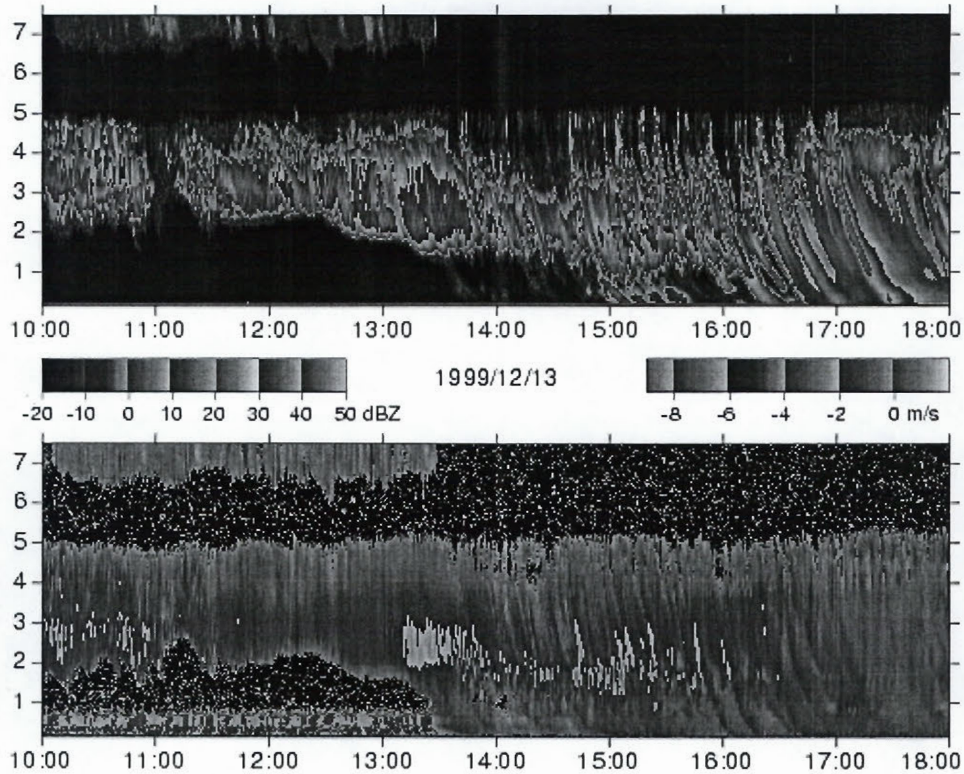

Figure 5.8: Time-height section of radar reflectivity (top) and vertical velocity (bottom) in precipitation. In this example, one observes mostly snow sublimating before it reaches the ground; however, the rapid velocities between 1300 and 1500 imply riming or SLW.

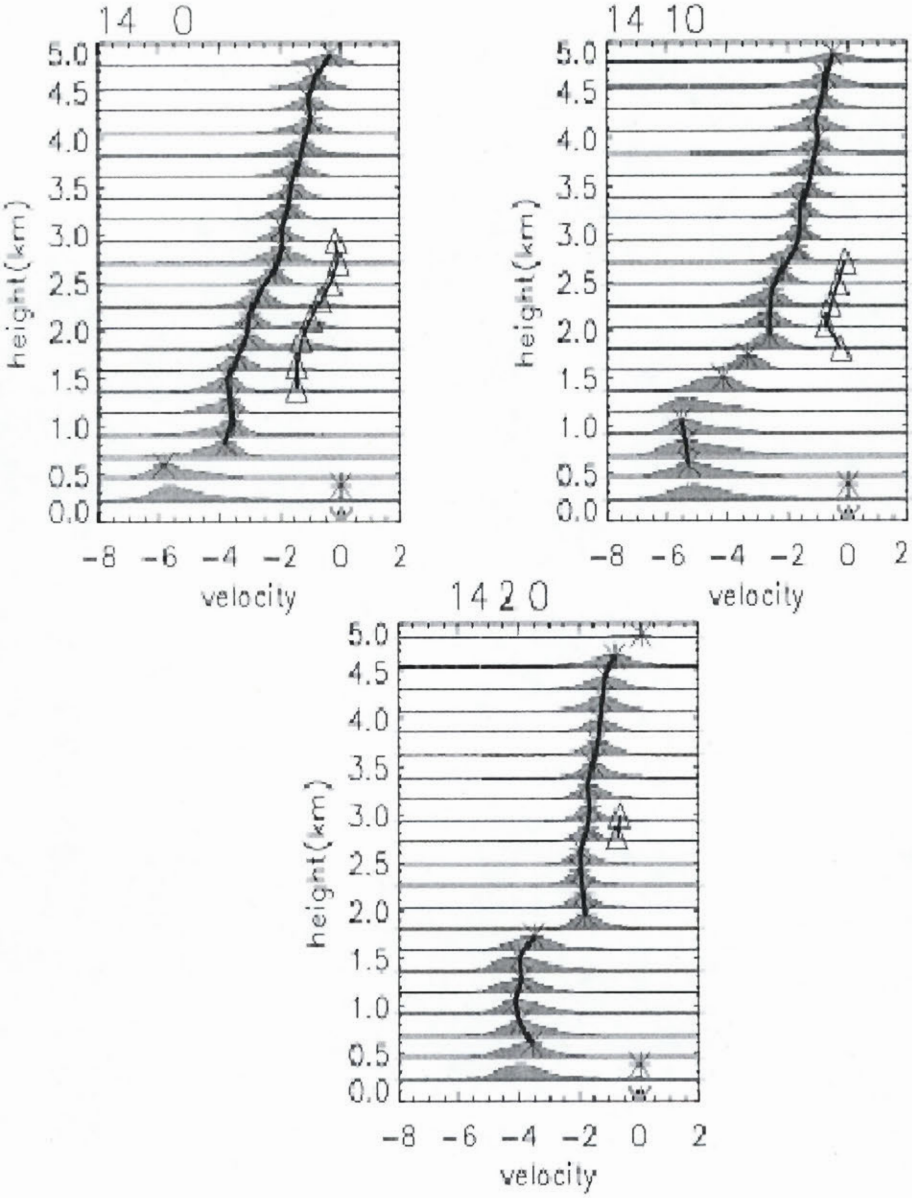

Figure 5.9: Spectra with clear secondary drizzle modes.

5.2.2 Classification to Final ID

Once the data has been separated into groups the next step was to apply the classification algorithms. The bright band algorithm was applied to the data in general first, and no bright band was found, which makes sense given the raw data (Fig. 5.8).

The results of the snowscore, rimescore, drizzlescore and rainscore algorithms are shown below in Fig. 5.10. Note the white region around 1400 where there is more than one mode. The score for this region is given by groups, but not shown in the image.

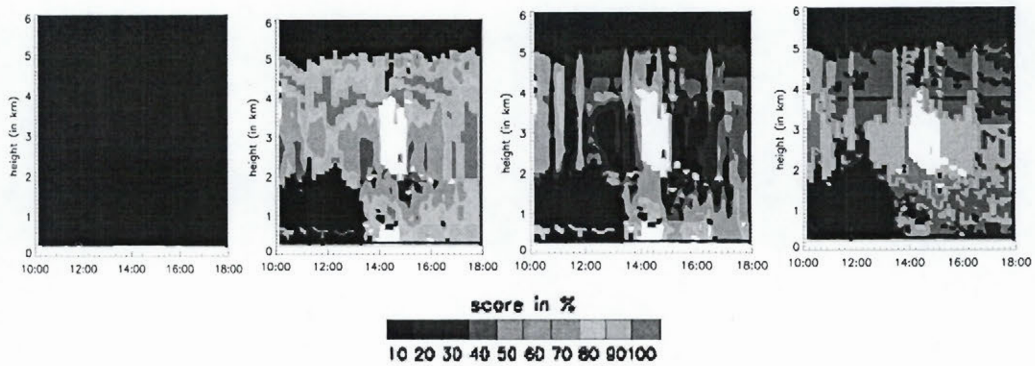

Rainscore Snowscore Drizzlescore Rimescore

Figure 5.10: From left to right are the fuzzy logic results of the rainscore, snowscore, drizzlescore and rimescore algorithms. The white areas are areas that had more than one mode and thus separate classifications must be done for each mode.

Next a final ID was given to the precipitation in each region, which is shown is Fig. 5.11. The final ID corresponds simply to the classification algorithms that have the highest score. In the cases with multiple groups, the final ID includes only the first group and all other groups were plotted (on the right panel of figure 5.11) as their own final IDs. In this case there is a final ID for the main and secondary groups.

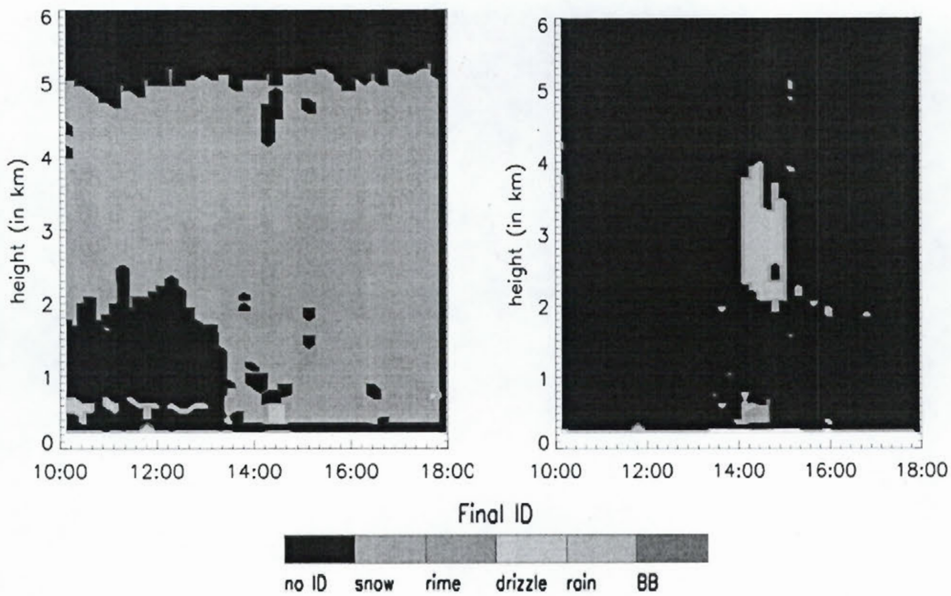

Figure 5.11: Final ID from classification algorithms on 12/13/99. The image on the right is the final ID for the secondary mode, while the image on the left is the final ID for the main mode. Like the spectra, this image shows the large secondary mode of drizzle basically surrounded by snow. In the main mode, the large patch of rime clearly shows how the SLW affects the snow.

5.2.3 Verification of Classification

As before the classification algorithms were verified with both surface and upper air data. Figure 5.12 shows a plot of the RH and temperature from Mirabel (YMX GRP118 1999), with any weather reported noted on top of the RH bars.

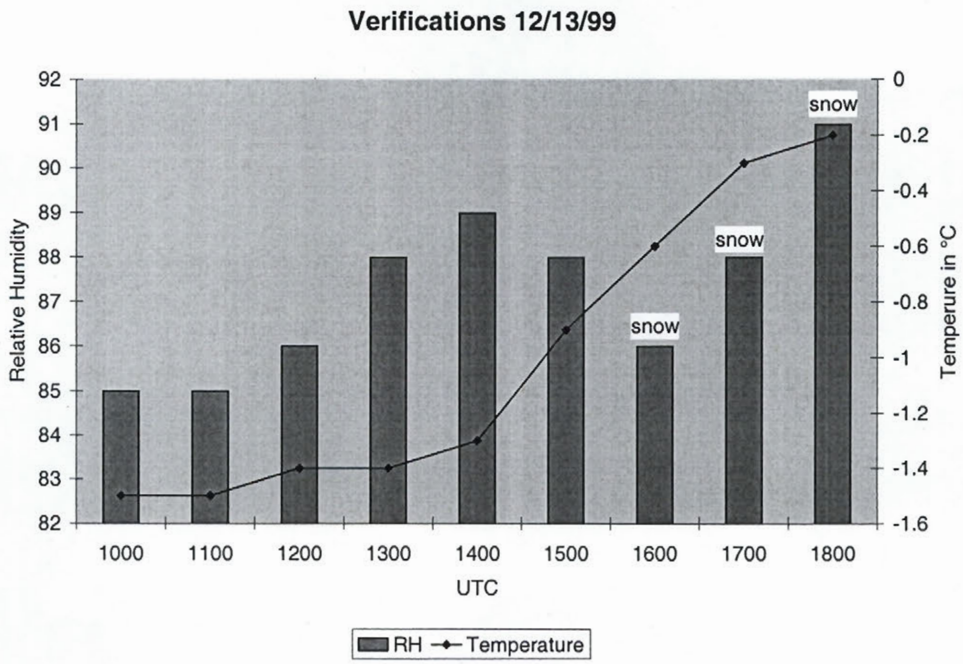

Figure 5.12: Surface observations of relative humidity and temperature from Mirabel. The reported weather is indicated above the relative humidity.

The raw VPR data implies precipitation aloft during the whole period; however, the reflectivity at the ground is below detectable levels until 1500. Thus it is not surprising that there are no surface observations of snow until 1600.

For more detailed information about any precipitation the radiometer is again considered. In this case, since the precipitation was snow the radiometer is a less accurate verification. The rain reported by the radiometer is likely a result of snow falling and melting onto its sensor. As shown below (Fig 5.13), the radiometer is reporting rain only in the last 45 minutes of the period when the temperature was the warmest and melting the most likely.

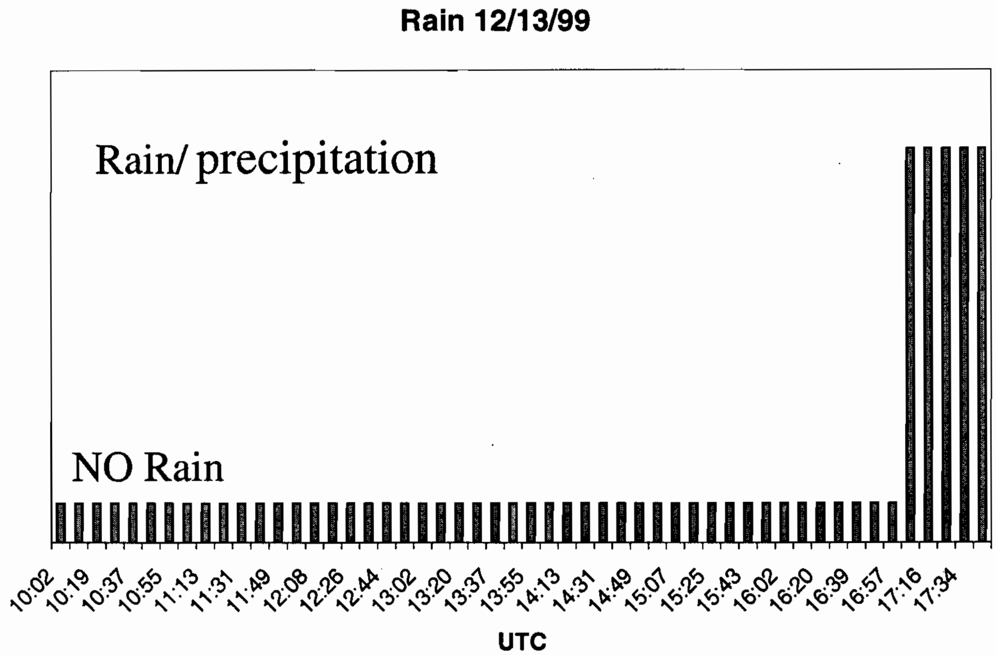

Figure 5.13: Rain occurrences from the TP/WVP3000 for 12/13/99

To confirm the upper level classification results, the sounding from 1416 UTC (Fig, 5.14) and 1714 UTC (Fig. 5.15) were used. The sounding at 1416 UTC offers a good insight into the vertical column above the airport. According to this sounding the column is saturated at the surface and then again above 2km. The entire sounding is below the 0°C isotherm; however, from 900hPa to 850hPa the temperature is isothermal and barely below 0°C. Just above that warm layer there is a 50hPa layer of very unstable but unsaturated air. From 2km to 5km the sounding is stable and saturated, then briefly conditionally neutral, and eventually dry above 500hPa. Since this sounding was taken at the beginning of a snowstorm the synoptic forcing also needs to be considered. Looking at the temperature trend from the surface observations (Fig. 5.12) an increasing trend in temperature is visible. This hints at the broader synoptic forcing causing updrafts and the liquid water above 2km. Superimposed on the broader synoptic lifting the sounding show regions of stable and unstable air resulting mostly from changes in saturation.

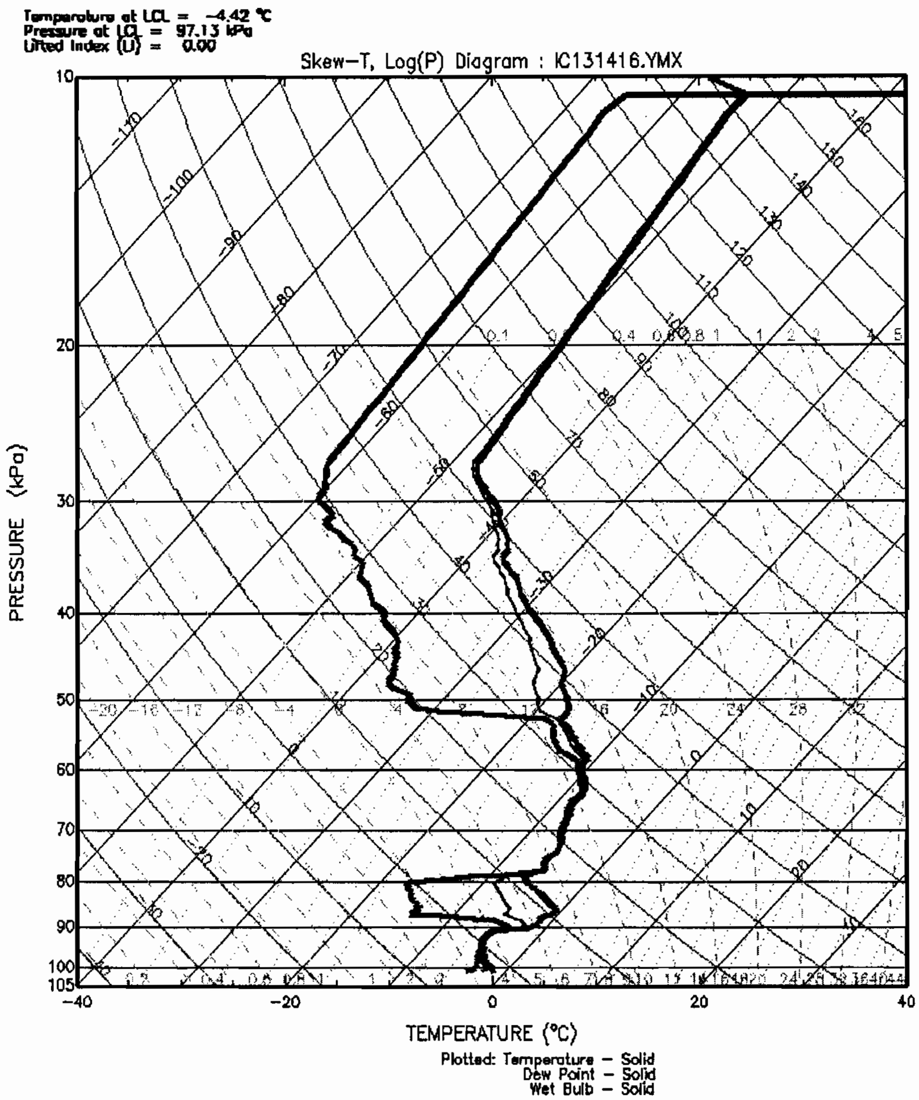

Figure 5.14: Sounding from 1416 UTC on 12/13/99.

A second profile taken at 1715 shows a much less complicated profile for the second half of 12/13/99:

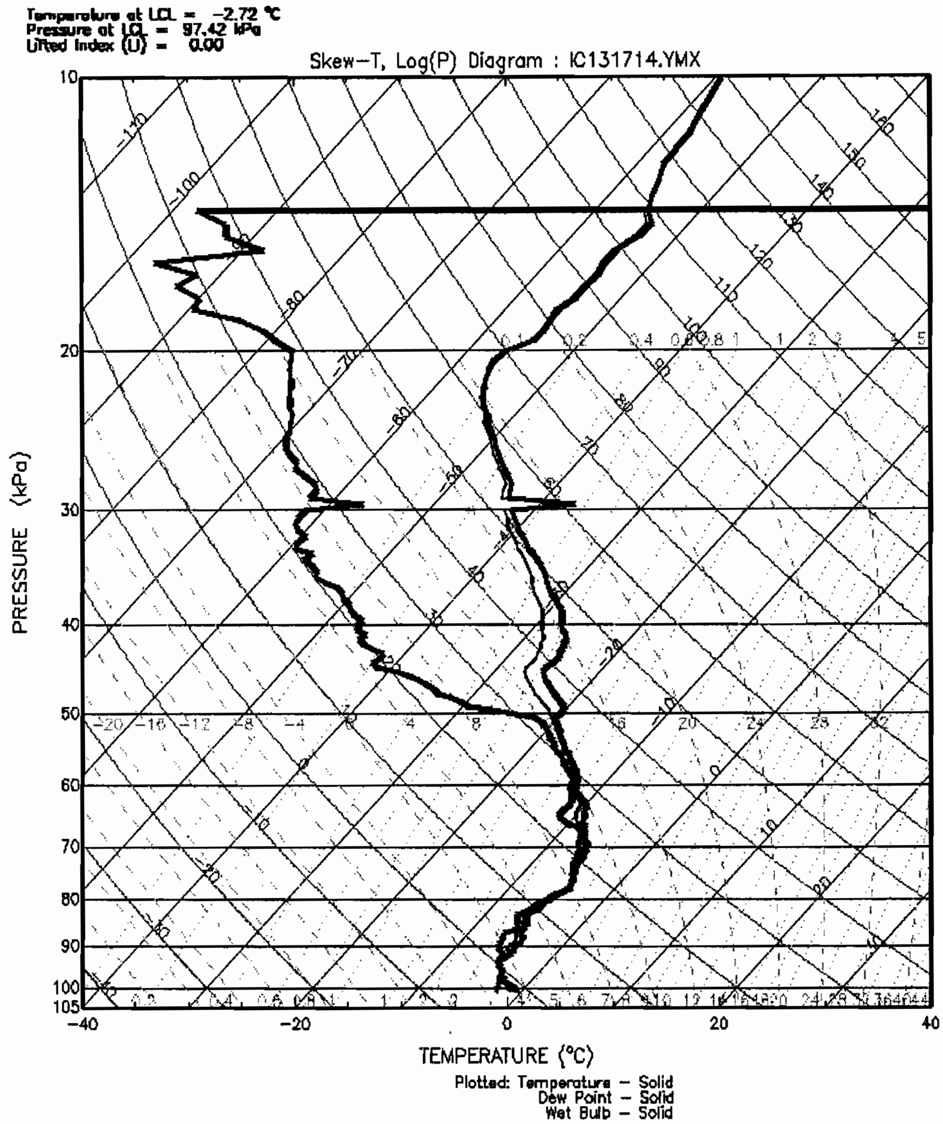

Figure 5.15: Sounding from 1714 UTC on 12/13/99.

In this sounding there is a stable, saturated layer, followed by a moist adiabatic layer, and eventually a dry layer above 500 hPa. The sounding is entirely below the 0°C isotherm and implies nothing more than simple snow.

Finally, photographs taken during the AIRS study can be used to confirm the riming indicated by the algorithm between 1400 and 1600. Photographs show actual rimed snowflakes falling to the ground. The first picture (Fig. 5.16) is taken at 1517 and shows both rimed and non rimed snowflakes. While this image is taken during the heavy riming period, most of the precipitation is still sublimating. The second picture is from 1740 and shows a much longer accumulation of snowflakes. In the second image there are rimed snowflakes, pristine flakes, and flakes that have partially melted since landing. It is impossible to tell from this image where the snowflakes originated.

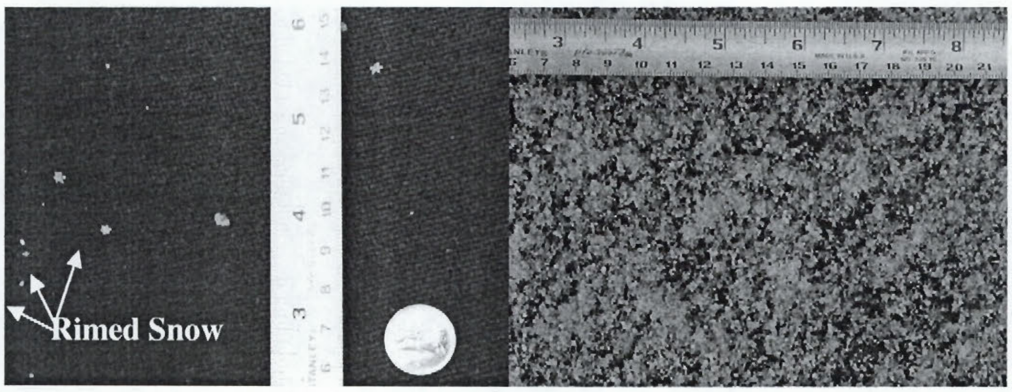

Figure 5.16: Photographs from 1517 and 1740 on 12/13/99. The right image shows rimed snowflakes, pristine flakes and some partially melted flakes. This image shows a much greater accumulation possibly because the accumulation rate is higher or possibly because the snow was allowed to collect for longer.

5.2.4 SFG and SDG Algorithms

The SFG and SDG algorithms were run when the final ID was either snow or rimed snow. Comparing the two images, the biggest difference to note is the additional LWC on the SFG plot around 1600.

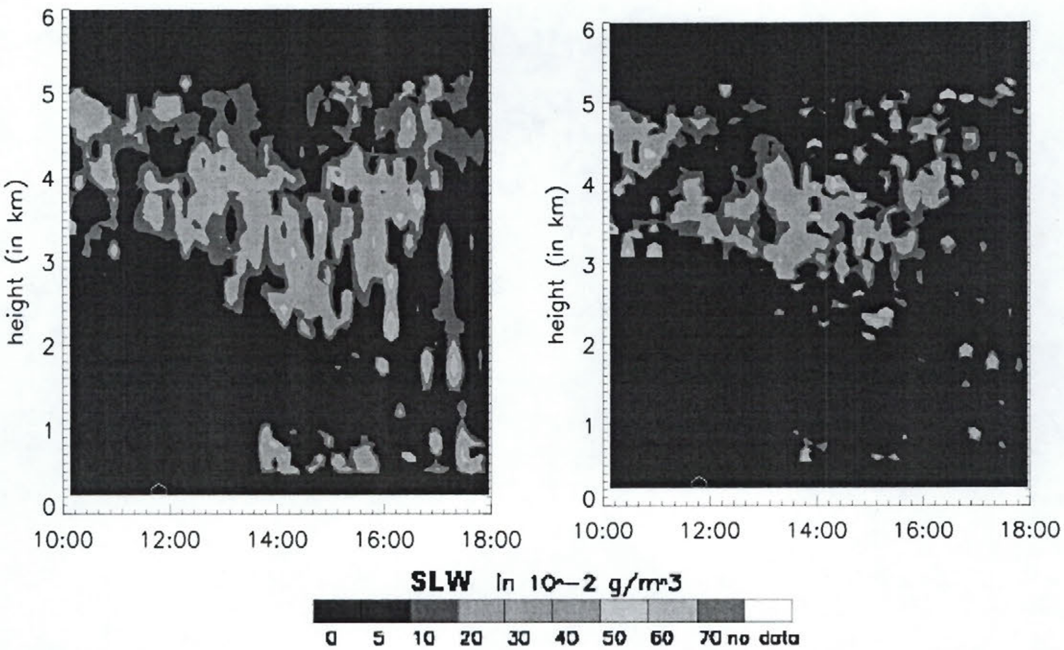

Figure 5.17: From left to right is the results of the SFG and SDG. While the two images are quite similar, the SDG has slightly higher results, and the SFG has slightly more areas with some LWC.

5.2.5 Verifications

To validate these results Fig. 5.18 shows a plot of integrated liquid water content (ILWC) from the SDF (pink), the SFG (yellow), and two radiometers, (light blue) the WVP-1100 radiometer and (dark blue) the TP/WVP3000. Again the SFG and SDG algorithm are fairly consistent with the SFG dominating everywhere except the very end. The dominance of the SFG is likely a result of aggregation caused by warmer temperatures.

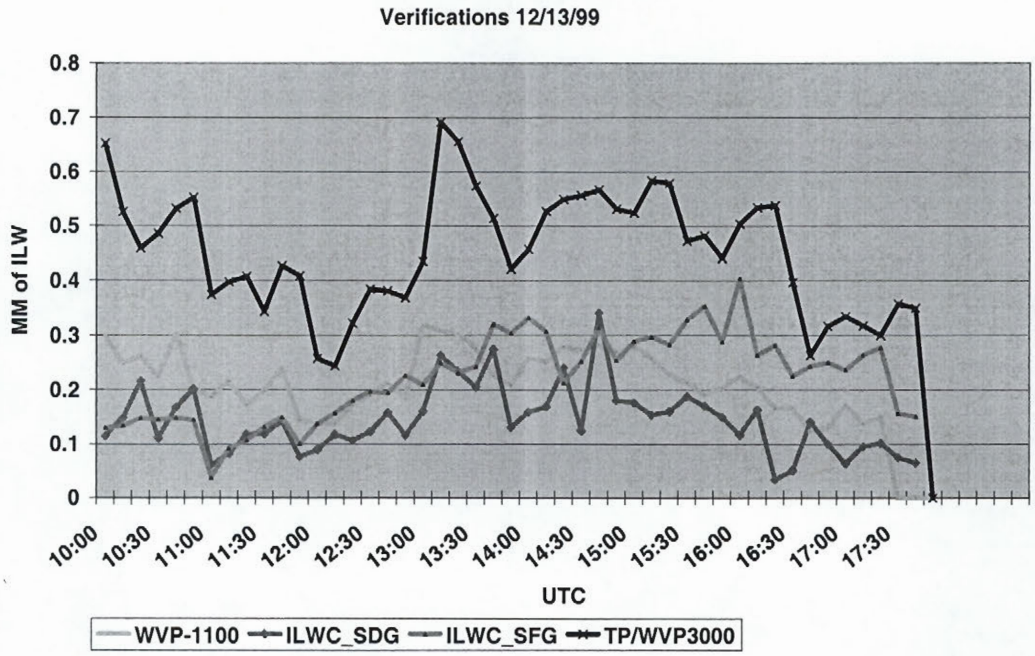

Figure 5.18: Verification of the SFG and SDG algorithms using integrated LWC from two radiometers.

5.3 December 16, 1999

5.3.1 Raw data/spectra

December 16th was another 24 hour period of interesting precipitation. While the temperatures on the ground were above freezing all day, the level of freezing remained around 500m according to the two soundings. The intensity of the precipitation ranged from nothing during the first two hours, to heavy precipitation between 0720 and 1400. The type of precipitation that fell during the heavier period is clearly different from the low level lighter precipitation that fell both before and after. The raw data are shown below in Fig. 5.19.

5.3.2 Classification to Final ID

Once the data was separated into groups, the classification algorithms were applied.

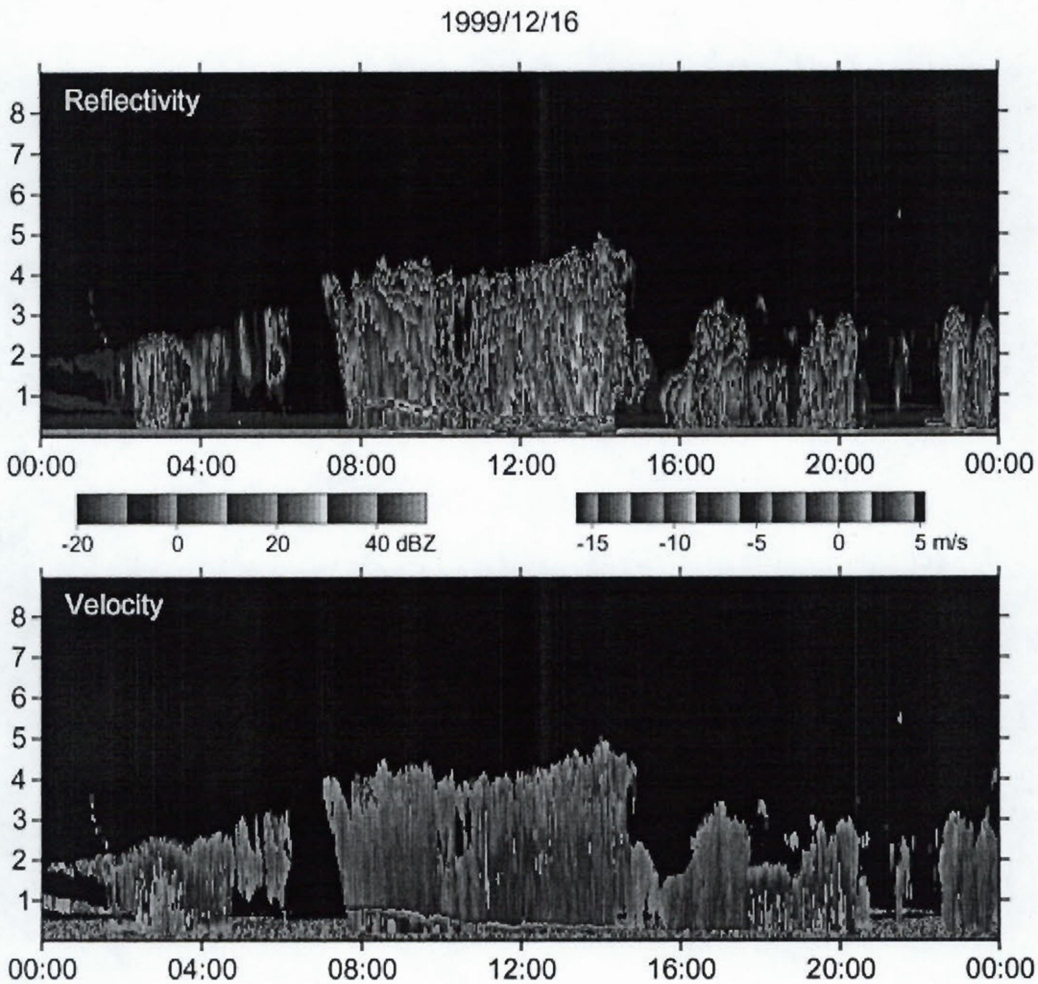

Figure 5.19: Time-height section of radar reflectivity (top) and vertical velocity (bottom) in precipitation. In this example, one can observe a variety of types of precipitation including snow, rain, and rime.

Plotting the spectra provides a more detailed look at the data. Spectra were plotted for the whole day, but there were no clear bi-modal areas. The first three spectra were taken from just before 400 when there is a sharp increase in velocity, and the second three spectra are taken just after the bright band begins.

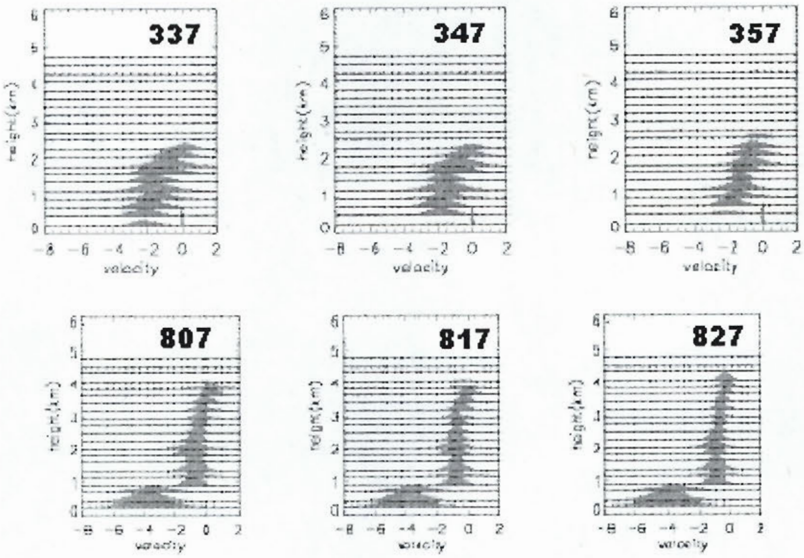

Figure 5.20: Spectra from 12/16/99

Plotting the bright band results provides a more detailed look at the freezing level than the two soundings can provide. The bright band (Fig. 5.21) shows that the freezing level, just below 1000m at 0600 falls towards the ground throughout the day.

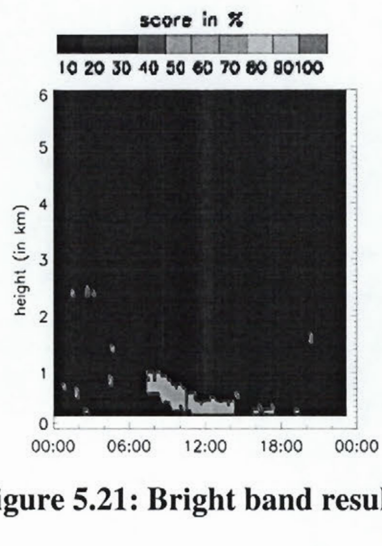

Figure 5.21: Bright band results

The results of the rainscore, snowscore, drizzlescore and rimescore algorithms are shown below in Fig. 5.22. There are few regions of overlapping modes, but it is clear that the fuzzy logic algorithms are finding many regions close to rime, snow and drizzle.

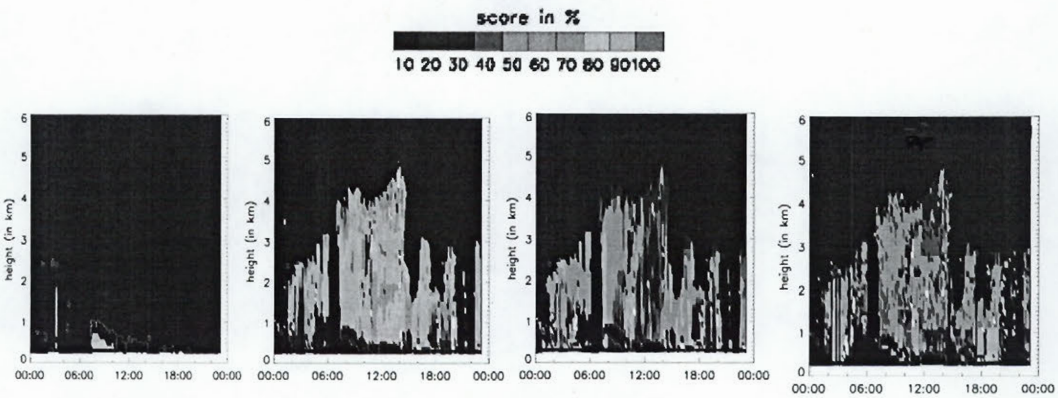

Rainscore Snowscore Drizzlescore Rimescore

Figure 5.22 From left to right are the fuzzy logic results of the rainscore, snowscore, drizzlescore and rimescore algorithms. The white areas are areas that had more than one mode and thus separate classifications must be done for each mode.

Next a final ID is given to the precipitation in each region which is shown is Fig. 5.23. The final ID corresponds simply to the classification algorithms that have the highest score.

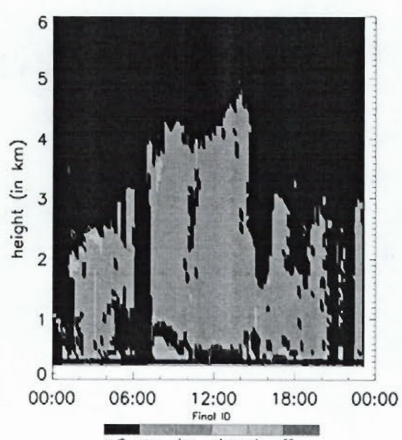

Figure 5.23: Final classification ID for 12/13/99.

5.3.3 Verification of Classification

As before the classification algorithms were verified with both surface and upper air data.

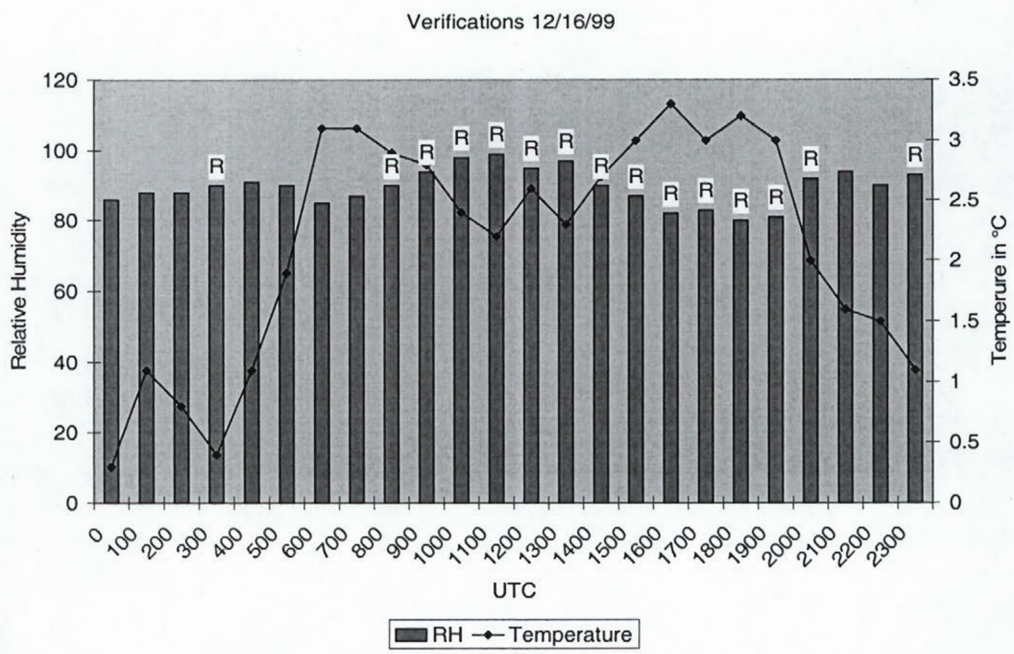

Figure 5.24: Surface observations of relative humidity and temperature from Mirabel. The reported weather is indicated above the relative humidity.

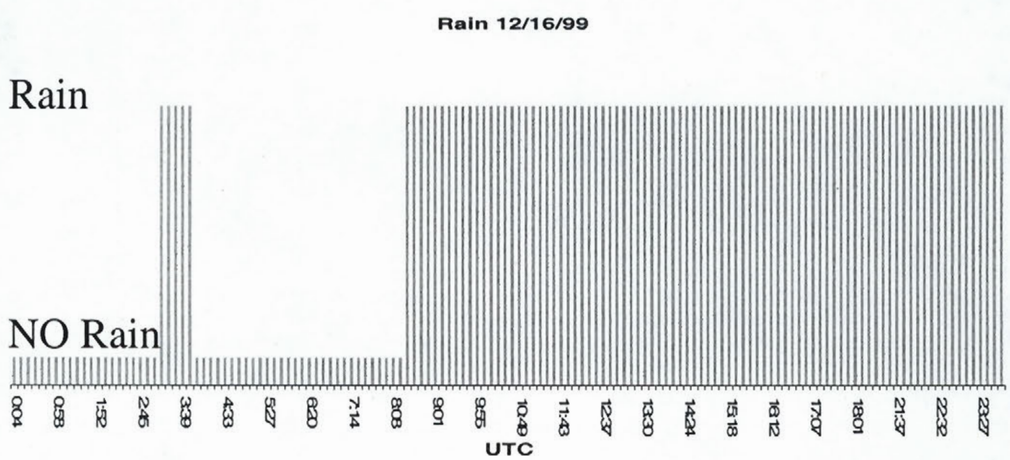

Figure 5.25: Rain occurrences from the TP/WVP3000 for 12/16/99

Figure 5.25 is the precipitation reported by the radiometer, which agrees well with the observations (Fig. 5.24) and the algorithms. To further verify the upper levels of the classification algorithms, soundings from 1117 UTC (Fig. 5.26 and 1415 UTC (Fig. 5.26) on December 16, 1999 were used.

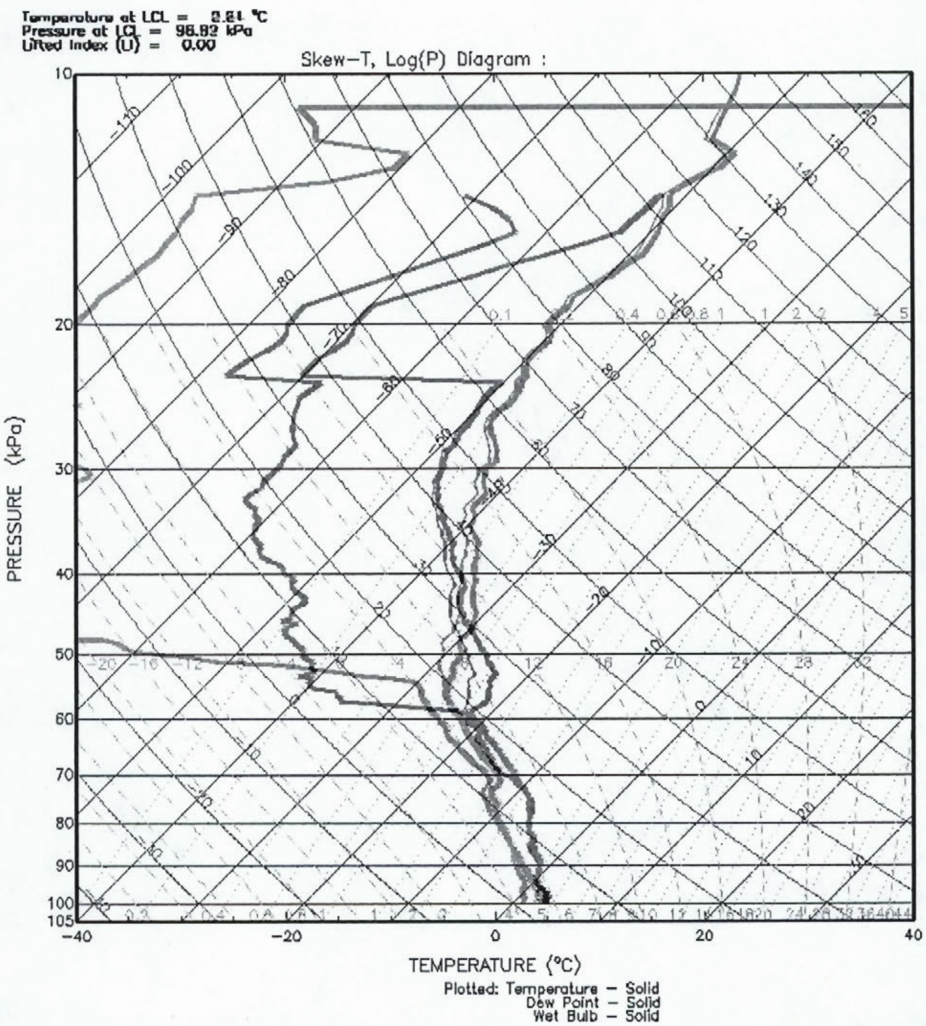

Figure 5.26: Sounding from 1115 UTC (grey) and 1415 (blue) on 12/16/99

The sounding from 1117 UTC (grey) was taken during a period with rain reported by the surface observation, the radiometer and the algorithms. At this point the bright band is very near the surface, around 500m in the algorithms. Accordingly the sounding crosses the 0°C isotherm at about 950 hPa or 500 m. The sounding is saturated and essentially moist adiabatic until 600 hPa. At this point, approximately 4 km it dried out, corresponding to the point were there is no longer any radar signal. The sounding from 1415 UTC (blue) was also taken in the rain, according to the radar, radiometer, and surface observations, and tells much the same story. However, the blue sounding is slightly cooler at the surface and slightly less stable. Up until about 3km the latter sounding is almost moist adiabatic, implying that any upward forcing would be enough to create SLW.

Photographs from December 16, 1999, also offer proof that at some point SLW is formed and the snowflakes were rimed. These two images taken 1 minute apart show the accumulation of rimed snowflakes at 1920, confirming the final ID claim of rimed snow from approximately 1800 to 2000.

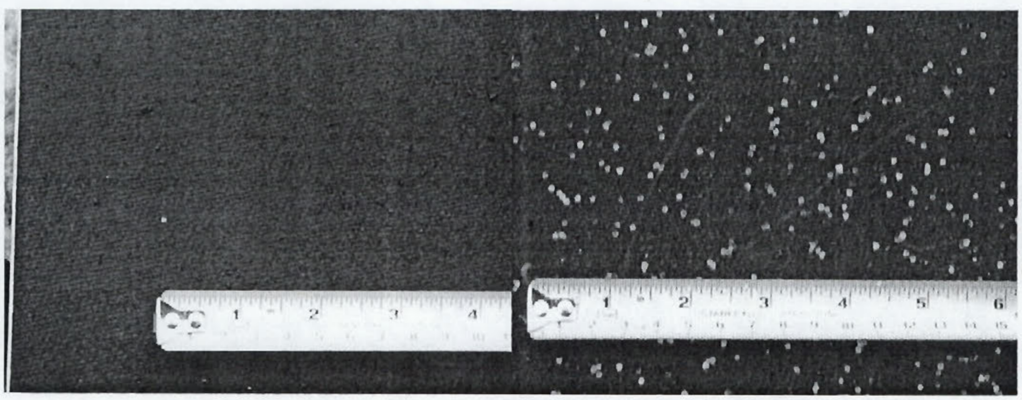

Figure 5.27: Photographs from 1920 and 1921 on 12/16/99. These two images show a 1 minute accumulation of rimes show at 1920 on 12/16/99.

5.3.4 SFG and SDG

The results of the SFG and SDG algorithms are show in Fig. 5.28. Comparing the two images, the biggest difference to note is the additional LWC on the SDG plot around 0300 and 1830.

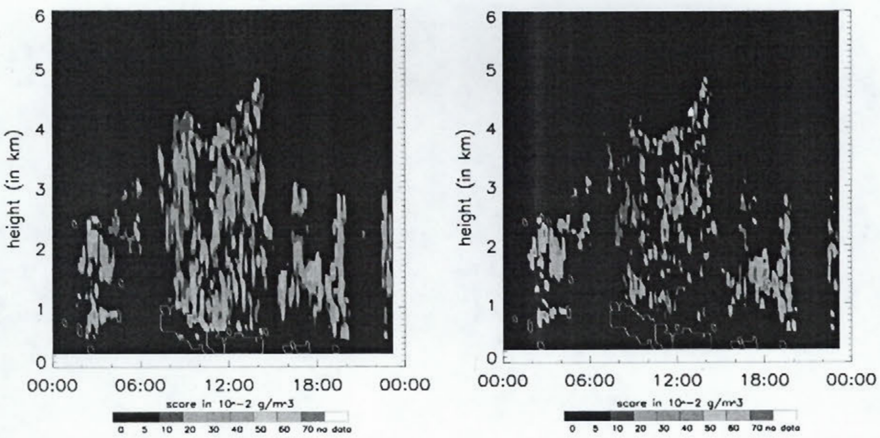

Figure 5.28: From left to right are the results of the SFG and the SDG algorithms. While the two images are quite similar, the SDG has slightly higher results, and the SFG has slightly more areas with some LWC.

5.3.5 Verifications

To validate these results integrated liquid water content (ILWC) from the SDF (pink), the SFG (yellow), and two radiometers, (light blue) is the WVP-1100 radiometer and (dark blue) is the TP/WVP3000 is plotted in Fig. 5.29.

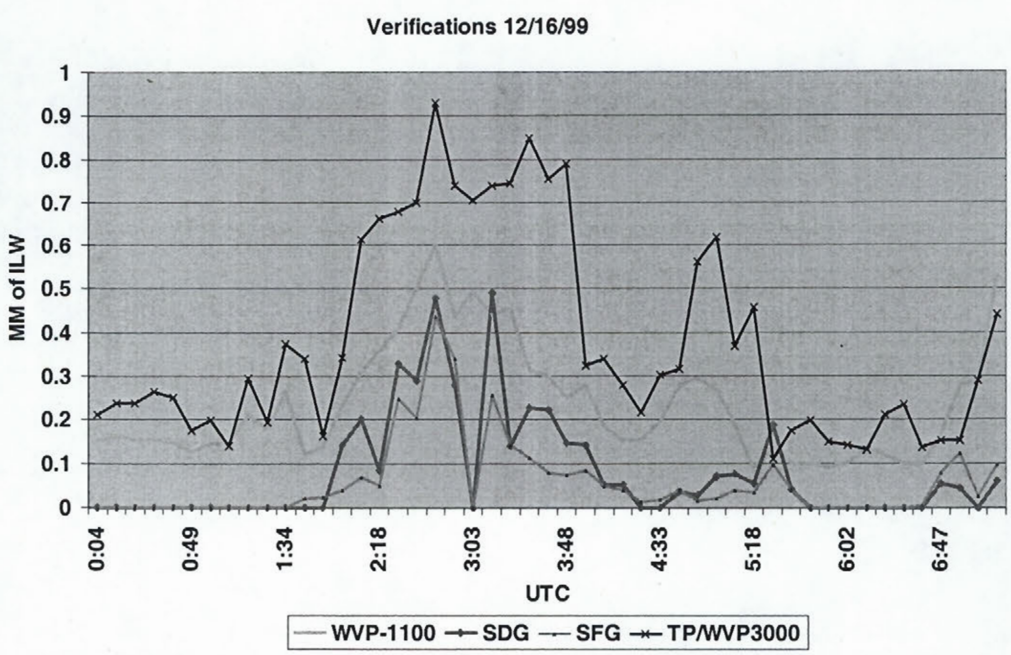

Figure 5.29: Verifications from 12/16/99

In this case the algorithms were run for all 24 hours; however the verifications are only shown for the first seven hours, since the radiometer data was not valid during periods when their sensors were wet.

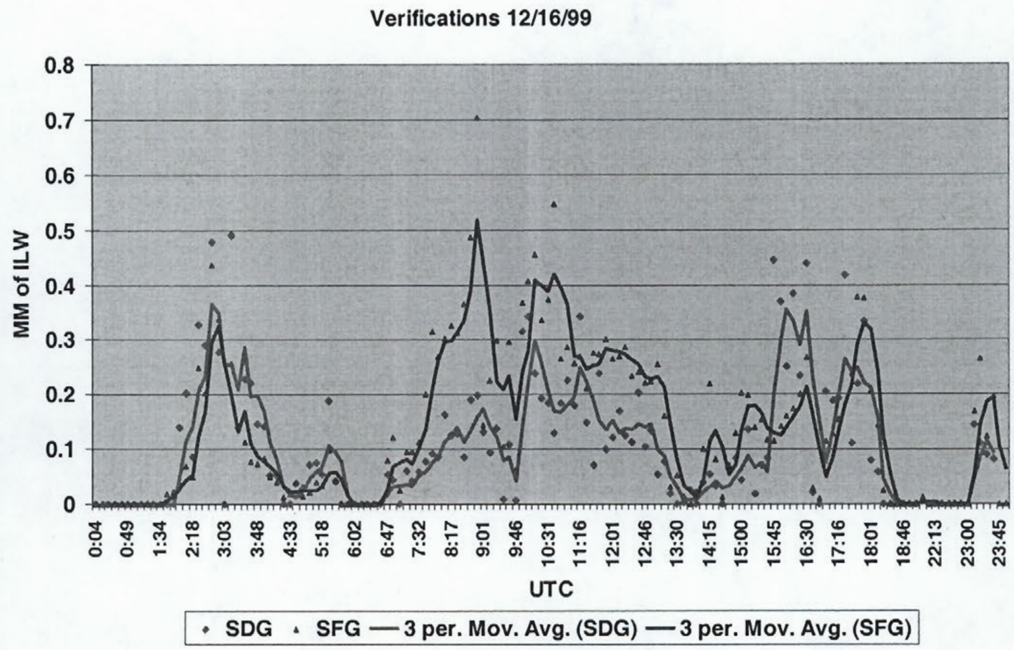

Figure 5.30: SFG and SDG averages compared over whole period

Again the SFG and SDG algorithm are fairly consistent over the whole period with the SFG dominating everywhere except for a short time between 0315 and 0430 and again between 1545 and 1630.

The three case studies presented in this chapter offer a verification of the work done in this study. The classification algorithms and final identification are shown to compare well against surface and upper level observations. With the success of the mode separation ID and classification algorithms the SFG and SDG algorithms are applied and tested. These two algorithms appear to be self-consistent and compare reasonably well with the radiometers.

Chapter 6

Conclusions

This study aimed to minimize icing dangers by creating a robust, real-time, accurate, automated system that uses VPR data and meteorological theory to reduce or even prevent icing-related aviation accidents. First, all mixed precipitation is separated. Then five fuzzy logic classification algorithms are applied to detect and distinguish different types of hydrometeors. Finally, the SLW content can be calculated within any regions of frozen precipitation with the Snow Flux Gradient (SFG) and the Snow Density Gradient (SDG) algorithms.

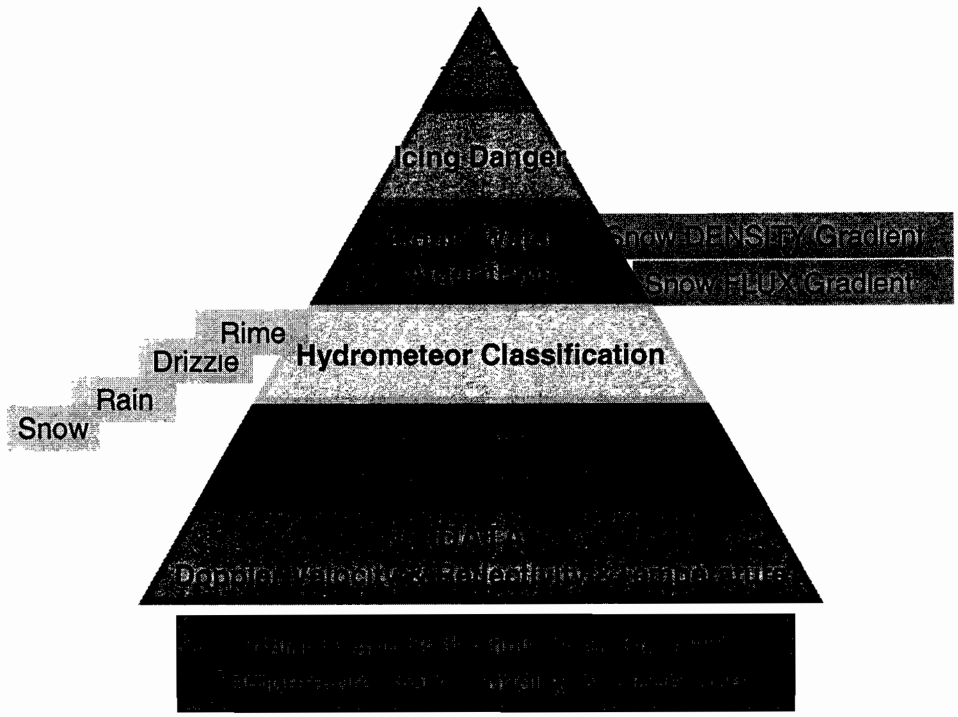

Figure 6.1: Overall schematic. Each step builds on the one below it, allowing a final calculation of icing danger.

To validate the results of the classification algorithms, surface observations, sounding, radiometer data, and aircraft data were used. Radiometric data is notorious for having unrealistically high values of ILWC when their sensors are wet, but in cases when it is not raining the radiometers have good agreement with both the algorithms. Using all other available data the classification algorithms were taken as performing well, with the possible exception of always being able to distinguish between drizzle and small snowflakes. For more general use of the algorithms, a possible solution is to add a decreasing dependence on reflectivity for drizzle with lower temperatures; since temperatures below zero rarely have drizzle with reflectivities above 0 dBZ.

Having accepted the classification algorithms, the next step of the project was to apply the SFG and SDG to regions to snow or rimed snow. These two algorithms are designed to calculate the LWC through changes in the mass flux or density when snowflakes co-exist with SLW. These changes allow the SFG and SDG algorithms can calculate how much liquid water is in a given region, and consequently how severe the icing will be on the aircraft.

Verifications of the calculated LWCs were done through the radiometer, soundings and when available aircraft data. In addition, it is reassuring to see the two algorithms generally agreed well with each other. Overall the SFG gave slightly larger values than the SDG, although it remained comparable with the radiometer values of ILWC. One possible explanation for the higher values of SFG is aggregation, which increases the size of particles and thus falsely increases the mass when mass is calculated though reflectivity. Another possible explanation of the high values of the SFG stem from the fact that this algorithm assumes that there the velocity of particles does not change (equation 4.6) which is untrue when a particle is rimed. The SDG also has some spikiness that may be a result of the way individual variable values were translated to bulk values for the calculations.

Finally, before expanding this study to general use it is worth noting that the spatial variability with which SLW exists in the atmosphere has yet to be determined. The special variability of LWC can affect the estimates made by this approach or any other approach that uses measurements obtained from a single vertical column. Still, the case studies and verification that have been shown in chapter 5 demonstrate the VPR potential when combined with the above algorithms to be not only accurate but also robust in its ability to identify icing in several different conditions. Before extending these algorithms to general use, continued verifications and modification need to be done, but with a little work, the use of these algorithms with a dedicated vertically pointing radar, alone or as part of a complex system, can hopefully be used to identify even the most complex icing situations.

Bibliography

1. AIRS I, 1999, Alliance Icing Research Study Science Plan, Available from <http://www.airs-icing.org>, Aug. 2004

2. Ahrens, C. D., 2000: *Meteorology Today: An Introduction to Weather, Climate, and the Environment*. 6th ed. West Publishing Company, 528 pp.

3. Austin, P M., A.C. Bemis, 1950:A Quantative Study of the "Bright Band" in Radar Precipitation Echoes. *Journal of the Atmospheric Sciences:* Vol. 7: 145-151

4. Bell, C., 2000: *Detection of the riming process with a vertically pointing radar*. M.Sc. thesis, McGill University.

5. Bellon, A., I. Zawadzki and F. Fabry, 1997: Measurements of melting layer attenuation at X-band frequencies. *Radio Sci.*, 943-955.

6. Cortinas Jr., John V., Bernstein, Ben C., Robbins, Christopher C., Walter Strapp, J. 2004: An Analysis of Freezing Rain, Freezing Drizzle, and Ice Pellets across the United States and Canada: 1976–90. *Weather and Forecasting*: Vol. 19, No. 2, pp. 377–390.

7. Côté, C., 2002: Detection of supercooled drizzle by a vertically pointing radar. Master's thesis, McGill University, 82pp.

8. Cunningham, Robert M. 1947: A Different Explanation of the "Bright Line". *Journal of the Atmospheric Sciences*: Vol. 4, No. 5, pp. 163–163.

9. D'Amico, M., C. Capsonl, and R. Nebuloni, 2000: A Melting Layer Model Investigated using Doppler Spectra, *Physics and Chemistry of the Earth*, VOL 25, No. 10-12, pp1069-1071

10. Driedger, N., J. Reid, G. Isaac, I. Gultepe, S. Cober, F. Fabry, 2004. GOES Subpixel Analysis Using AIRS-1.5 Remote Sensors. *Preprints, Eighth Symposium on Integrated Observing and Assimilation Systems for Atmosphere, Oceans, and Land Surface*, Seattle WA, 12-16 January 2004, Amer. Meteor. Soc., P1.4.

11. Douglas, R. H., K.L.S. Gunn, J.S. Marshall, 1957: Pattern in the Vertical of Snow Generation. *Journal of the Atmospheric Sciences*: Vol. 14, No. 2, pp. 95–114

12. Drummond, F.J., R.R. Rogers, S.A. Cohn, W.L. Ecklund, D.A. Carter, and J.S. Wilson, 1996: A New Look at the Melting Layer. *Journal of the Atmospheric Sciences*: Vol. 53, No. 5, pp. 759–769

13. Fabry, F., 1990: Precipitation Estimates by Radar, A Zenith Pointing Radar Perspective. Master's thesis, McGill University, 83pp.

14. -------- and I. Zawadzki, 1995: Long-term radar observations of the melting layer of precipitation and their interpretation. *Journal of the Atmospheric Sciences,* **52,** 838–851

15. ------- and W. Szyrmer, 1999: Modeling of the melting layer. Part II: Electromagnetic. *Journal of the Atmospheric Sciences*: Vol. 56, 3593–3600.

16. ------- and I. Zawadzki, 2000: Atmospheric physics as observed by a vertically pointing Doppler radar. *Proceedings, 13th International Conference on Clouds and Precipitation*, Reno NV, 310-313.

17. -------, I. Zawadzki, C. Bell, and C, Côté, 2001: Doppler Radar Signatures of In-Flight Icing Conditions. *30th International Conference on Radar Meteorology*, July 2001, Munich, Germany

18. -------, I. Zawadzki, S. Cober, G. Isaac, T. Ratvasky, F. Solheim, 2003: Detection of In-Flight Icing Conditions by Radar over an Airport. *FAA In-flight Icing / Ground De-icing International Conference & Exhibition*, June 2003, Chicago, IL, USA, **2003-01-2095**.

19. Fletcher, N., 1962: *The Physics of Rainclouds.* Cambridge University Press. 386pp.

20. Glickman, T.S., ED., 2000: *Glossary of Meteorology.* 2nd ed. American Meteorological Society., 855pp

21. Green, S.D., 2003: In-flight Icing Educational Objectives for Air Carrier Pilots. Paper AIAA 2003-21 41 *Aerospace Sciences Meeting and Exhibit 6-10* January 2003, Reno Nevada.

22. Gunn, R., and G. D. Kinzer, 1949: The terminal velocity of fall for water droplets in stagnant air. *J. Meteor.,* **6,** 243–248.

23. Hallett, J., G. Isaac, M. Politovich, D. Marcotte, A. Reehorst, and C. Ryerson, 2002: Alliance Icing Research Study II (AIRS II), Science Plan, December 2002. Available from < http://www.airs-

icing.org/AIRS_II/2003-01-06_AIRS_II_Science_Plan.pdf>, Aug. 2004

24. Hartman, E.P., 1970; Adventures in Research, A History of the AMES Research Center 1940-1965, NASA Center History Series, Scientific and Technical Information Division, office of technology utilization, National Aeronautics and Space Administration, Washington, D.C.

25. Isaac, G., S. Cober, J.W. Strapp, D. Hudak, T.P. Ratvasky, D.L. Marcotte and F. Fabry, 2001a: Preliminary results from the Alliance Icing Research Study (AIRS). *AIAA 39th Aerospace Sciences Meeting & Exhibit*, 8-12 January 2001, Reno, Nevada

26. --------, -------, -------, A.V. Korolev, A. Tramblay, and D.L. Marcotte, 2001b: Recent Canadian research on aircraft in-flight icing, *Canadian Aeronautics and Space Journal*, **47,** #3, 213-221.

27. Joss, J. and A. Waldvogel, 1970: Raindrop size distribution and Doppler velocities. *14th Radar Meteorology Conference,* Tucon, Amer. Meteor Soc. 153-156

28. Kessler, E., 1969: *On the Distribution and Continuity of Water Substance in Atmospheric Circulation.* American Meteorological Society Meteor. Monogr., No. 32,.., 84 pp.

29. Koenig, L.R., 1972: Parameterization of Ice Growth for Numerical Calculations of Cloud Dynamics. *Monthly Weather Review*: Vol. 100, No. 6, pp. 417–423.

30. Korolev, A. V., M.P. Bailey, J. Hallett, G.A. Isaac, 2004: Laboratory and In Situ Observation of Deposition Growth of Frozen Drops. *Journal of Applied Meteorology*: Vol. 43, No. 4, pp. 612–622.

31. Le Bot, C. 2003: SIGMA: System of Icing Geographic identification in Meteorology for Aviation, *FAA In-flight Icing / Ground De-icing International Conference & Exhibition*, 2003-01-2085.

32. Mack, P.E., ed. *From Engineering Science to Big Science.* The NASA History Series, National Aeronautics and Space Administration, NASA Office of Policy and Plans, NASA History Office, Washington, D.C. 1998

33. Marshall, J. S., 1953: Precipitation Trajectories and Patterns. *Journal of Meteor.,* **10,** 25-29

34. Marshall, J. S., R.C. Langille, and W. M. Palmer, 1948: Measuring rainfall by radar. *J. Meteor.*,**4,** 186–192

35. Mitchell, David L., Zhang, Renyi, Pitter, Richard L. 1990: Mass-Dimensional Relationships for Ice Particles and the Influence of Riming on Snowfall Rates. *Journal of Applied Meteorology*: Vol. 29, No. 2, pp. 153–164.

36. National Transportation Safety Board (NTSB). 2004: Available from <http://www.ntsb.gov/aviation/Table10.htm data> Aug. 2004

37. Petty, K.R., J.T. Skeen, Jr., G.D. Salottolo, and C.D.J. Floyd. 2003: The Role of the NBTS in Aviation Icing Accident Investigations. *FAA In-flight Icing / Ground De-icing International Conference & Exhibition*, 2003-01-2086.

38. Paull, G., and E. Hagy, 1999: Historical overview of in-flight icing accidents. Management Consulting Research Federal Tech. Rep. TR-9854/01-1, 43 pp. [Available from Management Consulting Research Federal, Inc., 175 Middlesex Turnpike, Bedford, MA 01730.

39. Pocernich, M., C. Wolff, and T. Fowler, 2004: Statistical Models of Aircraft Icing, *17th Conference on Probability and Statistics in the Atmospheric Sciences,* January 2004, Seattle, Washington

40. Pruppacher, H.R., and J.D. Klett, 1997: *Microphysics of Clouds and Precipitation.* Kluwer Acidemic. Publishers, 945pp.

41. Rasmussen, R., M. Dixon, F. Hage, J. Cole, C. Wade, J. Tuttle, S. McGettigan, T. Carty, L. Stevenson, W. Fellner, S. Knight, E. Karplus, N. Rehak. 2001: Weather Support to Deicing Decision Making (WSDDM): A Winter Weather Nowcasting System. *Bulletin of the American Meteorological Society*: Vol. 82, No. 4, pp. 579–596.

42. Reehorst, A., J.Chung, M.Potapczuk and Y. Choo, 2000: Study of icing effects on performance and controllability of an accident aircraft. *J. Aircraft, 37,* 253-259.

43. ---------- and M.K. Politovich. 2003: Development of Icing Condition remote Sensing Systems and their Implications for Future Flight Operations. *FAA In-flight Icing / Ground De-icing International Conference & Exhibition*, 2003-01-2096.

44. Rinehart, R. E., 1997: *Radar for Meteorologists*, third edition, Rinehart Publications, 428pp.

45. Reinking, R.F., R. A. Kropfli, S. Y. Matrosov, W. C. Campbell, M. J. Post, D. A. Hazen, J. S. Gibson, K. P. Moran , and B. E. Martner, 2001: Concept and Design for a pilot Demonstration group-Based remote icing detection system, *30th International Conference on Radar Meteorology*, July 2001, Munich, Germany

46. Rogers, R. 1964: An Extension of the Z-R relation for Doppler radar. *11th weather radar conference,* Bolder, American Meteorological Society 158-161.

47. --------, and M. Yau, 1996: *A Short Course in Cloud Physics.* Pergamon Press 294pp.

48. Ryerson, C., L. Peck, and C.J. Martel, 2003: Army Aviation Operations in Icing Conditions. *FAA In-flight Icing / Ground De-icing International Conference & Exhibition*, 2003-01-2094.

49. Sand, W.R., W.A. Cooper, M.K. Politovich, and D.L. Veal, 1984: Icing Conditions Encountered by a Research Aircraft. *Journal of Applied Meteorology*: Vol. 23, No. 10, pp. 1427–1440.

50. Sauvageot, H., 1992: *Radar Meteorology.* Artech House, 366 pp.

51. Sekhon, R.S., Srivastava, R.C.. 1970: Snow Size Spectra and Radar Reflectivity. *Journal of the Atmospheric Sciences*: Vol. 27, No. 2, pp. 299–307.

52. Sheppard, B. E. 1990: Measurement of Raindrop Size Distributions Using a Small Doppler Radar. *Journal of Atmospheric and Oceanic Technology*: Vol. 7, No. 2, pp. 255–268.

53. Steiner, M. 1991: A New Relationship between Mean Doppler Velocity and Differential Reflectivity. *Journal of Atmospheric and Oceanic Technology*: Vol. 8, No. 3, pp. 430–443.

54. Strapp, J.W., R.A. Stuart and G.A. Isaac, 1996: Canadian climatology of freezing precipitation, and a detailed study using data from St. John's, Newfoundland. *FAA International Conference on Aircraft In-flight Icing*, May 1996, Springfield, Virginia, Volume II, DOT/FAA/AR-96/81, 45-55.

55. Stewart, R.E., J.D. Marwitz., J.C. Pace, R.E. Carbone,. 1984: Characteristics through the Melting Layer of Stratiform Clouds. *Journal of the Atmospheric Sciences*: Vol. 41, No. 22, pp. 3227–3237.

56. ------- and G.A. Isaac, 1999: Freezing Precipitation in Canada. *Atmosphere Ocean*, 37-1, pp.87-102.

57. Tafferner, A., Hauf, T., Leifeld, C., Hafner, T., Leykauf, H., Voigt, U. 2003: ADWICE: Advanced Diagnosis and Warning System for Aircraft Icing Environments. *Weather and Forecasting*: Vol. 18, No. 2, pp. 184–203.

58. Večei, D., 2002: Detection of Supercooled cloud by Radar: Algorithm Comparisons with Aircraft data, Master's thesis, McGill University, 84pp..

59. Weiss, R., and P. Hobbs, 1974: The Use of a Vertically Pointing Pulsed Doppler Radar in Cloud Physics and Weather Modification Studies, *Journal Of Applied Meteorology,* **14**, 222-231

60. Xue, X., 1999: Observations and data analysis of supercooled liquid water, Master's thesis, McGill University.

61. Zadeh, Lotfi Asker, 1987: *Fuzzy sets and applications : selected papers / by L.A. Zadeh ;* edited by R.R. Yager ... [*et al.*], New York Chichester John Wiley & Sons c1987

62. Zawadzki, I., P. Zwack, and A. Frigon, 1993: A study of a CASP storm: Analysis of radar data, *Atmosphere-Ocean,* **31**, 201-233

63. ---------., and F. Fabry, 2000A: Detection of supercooled water by a low-cost X-band vertically pointing radar. *Bull. Amer. Meteor. Soc.*, submitted.

64. -------- and F. Fabry, 2000B: Observations of supercooled water and of secondary ice generation by a vertically pointing X-band Doppler radar. Proceedings, 13th International Conference on Clouds and Precipitation, Reno NV, 264-267.

65. --------, Szyrmer, W., Laroche, S. 2000: Diagnostic of Supercooled Clouds from Single-Doppler Observations in Regions of Radar-Detectable Snow. *Journal of Applied Meteorology*: Vol. 39, No. 7, pp. 1041–1058.

66. Zeng, Z, S.E. Yuter, R.A. Houze, D.E. Kingsmill, 2001: Microphysics of the Rapid Development of Heavy Convective Precipitation. *Monthly Weather Review*: Vol. 129, No. 8, pp. 1882